Construction of a Wide-Field Optical Sectioning Microscope

Master's thesis by
Tobias Wiesel

Lund Reports on Atomic Physics, LRAP-317
Lund, January 2004

ABSTRACT

We have constructed a wide-field microscope, which uses structured light to obtain optical sectioning with properties similar to those of a confocal microscope. The work has involved optical and opto-mechanical design as well as some software development for computer control of the instrument and analysis of data. The system has been tested on stationary objects. It has been found that the result is highly depending on the signal-to-noise ratio of the images acquired. The intension is to use this instrument to study the morphology of red blood cells under the influence of different flow rates within a near future. The work was conducted within the scope of a Master's project.

TABLE OF CONTENTS

1 INTRODUCTION

This thesis is the result of a Master's project at the Atomic Physics department at Lund Institute of Technology. My work was conducted under supervision of Prof. Stefan Andersson-Engels at the group for medical applications.

Molecular imaging is an interesting and quickly emerging new field in diagnostic medicine. It involves probes, targeting molecules expressed specifically under certain tissue conditions. One way to detect the specific probes used in molecular imaging is with optical methods. Thus, optical microscopy is a growing field of molecular imaging. To keep up with the development within this field, we wanted to get into a method, which provides optical sectioning with confocal properties using an optical microscope with structured illuminating, presented by Neil et. al..[1]

The primary objective of the project was to construct such a microscope. A secondary objective was to apply this instrumentation in studies of the dynamic morphology of red blood cells flowing through a thin cuvette. These properties are, due to their effect on the optical properties of the blood, of importance in many types of optical measurements of blood. The red blood cells are interesting to study since it is, to some extent, possible to control their morphology by applying a controlled flow rate.

The objectives of the project were realized in different steps. First of all, a literature search was made to find out what has previously been carried out in this field of optical sectioning microscopy. Then a microscope, based on Neil et. al.'s method, was constructed to image stationary objects. This microscope would later be reconstructed to meet the secondary objective to acquire images of flowing blood.

The development of microscopes, based on the method above, has previously been concentrated to fluorescence microscopy. These fluorescence measurements have also been combined with fluorescence lifetime[2,3] and hyperspectral imaging.[4,5,6] However, this is, to our knowledge, the first attempt to study moving objects with this method of optically sectioning microscopy.

The outline of this thesis begins with an introduction to tissue optics in ***Chapter 2***, which describes absorption and scattering in turbid media. The special characteristics of blood are discussed in ***Chapter 3***. This is followed by a general discussion of microscopy in ***Chapter 4***, which leads the reader into the field of confocal microscopy and optical sectioning. A description of the system design and its performance are found in ***Chapters 5*** and ***6*** followed by the measurement results in ***Chapter 7***.

2 TISSUE OPTICS

Light that is sent into biological tissue can be exposed to different processes. Below reflection at and transmission through the tissue surface are described followed by a discussion on absorption and scattering inside the tissue. The last section in this chapter describes some mathematical models of light distribution in tissue.

2.1 Reflection and transmission

Light incident to tissue can, from a macroscopic point of view, either be reflected or transmitted at the tissue surface. This can easily be demonstrated by pointing a torch at the palm of your hand. Some of the light can be seen looking at the palm, this is a combination of specular and diffuse reflection, and some transmitted light can be seen on the dorsal side of the hand. A fraction of the light that hits a tissue surface is reflected and the rest is transmitted into the tissue, refer to ***Figure 1***. The amount that is reflected depends on the angle of incidence and refraction index.

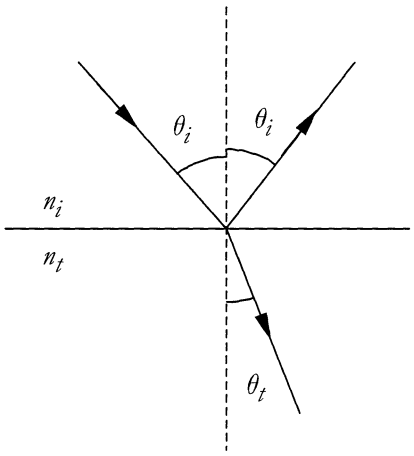

Figure 1: ***Transmission and reflection at the interface between two media with different refraction indices.***

Due to the difference in refraction indices, n_i for the surrounding medium and n_t for the tissue, the transmitted light is deflected. (i and t indicates incident and transmitted light respectively) The surrounding medium is often air that has a lower refraction index than do biological tissue. According to *Snell's law of refraction*,

$$n_i \sin\theta_i = n_t \sin\theta_t, \tag{1}$$

the transmitted light is deflected towards the normal to the surface.[7] The relation between the reflection coefficient, r, the angle of incidence, θ_i, and the refraction angle, θ_t, is given by the *Fresnel reflection equations,*

$$r_{\perp} = \frac{n_i \cos\theta_i - n_t \cos\theta_t}{n_i \cos\theta_i + n_t \cos\theta_t} \tag{2a}$$

$$r_{||} = \frac{n_t \cos\theta_i - n_i \cos\theta_t}{n_i \cos\theta_t + n_t \cos\theta_i}. \tag{2b}$$

In these equations, which can be derived from the theory of electromagnetic radiation,[7, 8] $\perp$ and $||$ indicate that the **E**-field is perpendicular and parallel, respectively, to the plane of incidence. It has also been shown that the Fresnel equations can be reduced to

$$r_{\theta_i=0} = \left[r_{||}\right]_{\theta_i=0} = \left[-r_{\perp}\right]_{\theta_i=0} = \frac{n_t - n_i}{n_t + n_i} \tag{3}$$

at normal incidence of the light.[7, 8]

The reflectance, R, is defined as the ratio of the reflected power to the incident power, which can also be expressed as the square of the reflection coefficient.[7] Thus, when illuminating tissue, approximated to be homogenous with a refraction index of 1.4, the specular reflectance can be calculated to 0.028. This means that 2.8 % of the incident light is reflected directly at the surface between air and tissue. Since $T = 1 - R$ it follows that the ratio of light transmitted into the tissue is 0.972 or 97.2 %.

The total reflected light comprises both specular reflection, light reflected directly at the illuminated surface as described above, and diffuse reflection, light re-emitted through the surface after a number of scattering events inside the tissue (scattering will be discussed later). This is one reason why the total reflected light ratio exceeds the reflectance. Other reasons are divergence of a laser beam and roughness of the tissue surface.

2.2 Absorption

The total attenuation in a turbid medium depends on both absorption and scattering by the atoms, molecules and small tissue structures inside the medium.[9] Absorption in tissue is discussed below and scattering will be described in ***Section 2.3***.

When a photon and an atom meet, the photon can be absorbed if its energy corresponds to the electronic energy structure of the atom. Consider a vessel containing an absorbing, non-scattering medium. A collimated light beam with a specific intensity is directed towards the substance (at normal incidence). The light intensity is attenuated when measured on the other side of the vessel. This attenuation depends on the absorption coefficient, denoted μ_a [cm^{-1}] of the substance. The light intensity throughout the medium is described by the *Beer-Lambert law*,[7] which states that the intensity is exponentially attenuated according to

$$I = I_0 \exp(-\mu_a z). \tag{4}$$

I is the attenuated intensity, I_0 is the initial intensity and z is the distance the light has travelled in the medium. The attenuation due to Beer-Lambert law is illustrated in ***Figure 2***.

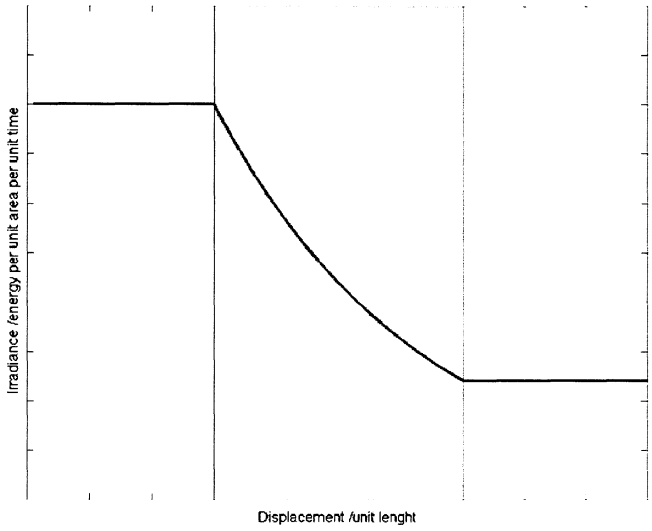

Figure 2: ***The Beer-Lambert law states that the intensity of light passing through an absorbing, non-scattering medium is attenuated exponentially. The grey area illustrates the homogeneous medium.***

The absorption coefficient should be interpreted as the probability of an event of absorption per unit length.[10] The inverse of μ_a gives the absorption mean free path length, i.e. the average distance a photon travels before it is absorbed. The absorption coefficient, as well as the scattering coefficient, varies widely depending on the wavelength of the light. The absorbing molecules in biological tissue, so called chromophores, have different absorption spectra. *Water*, for example, absorbs strongly in the UV-region below 200 nm and in the near-IR- and IR-regions above 700 nm.[11] In between these regions the water absorption is low compared to other chromophores' absorption. The absorption spectrum for water is shown in ***Figure 3***.

Haemoglobin, which is the oxygen carrying pigment in the red blood cells, has a quite complex absorption signature with rather high absorption in the visible wavelength region, 380 nm and 770 nm, see ***Figure 3***.[12] The difference in the absorption spectra of oxy- and deoxy-haemoglobin, i.e. oxygenated and deoxygenated haemoglobin respectively, can be used e.g. to measure blood oxygenation, as in pulse-oximetry.[13]

Figure 3 shows, as mentioned above, the absorption spectra for water and haemoglobin. Due to that the absorption of most tissue chromophores is low in the red and near-IR region, this region is called the tissue optical window. Since the absorption is low it is advantageous to use light in this region if a good penetration depth is wanted. Note that the chromophore concentrations in the figure are not related to each other. The water curve holds for 25°C and a haemoglobin concentration of 150 g/litre, which is a typical value for whole blood, is used.

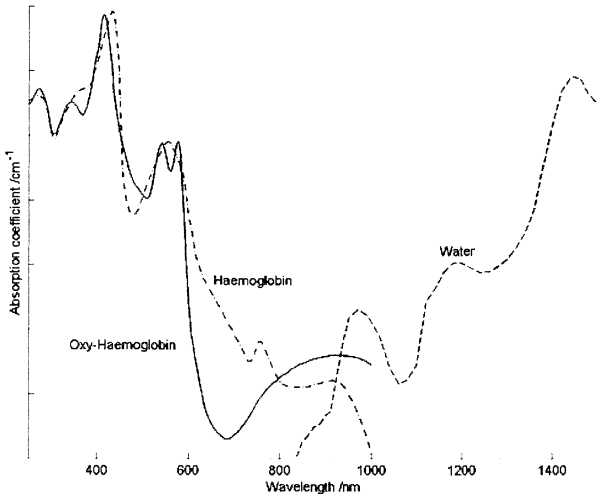

Figure 3: ***Absorption spectra for water[11] and oxygenated and deoxygenated haemoglobin[12]. There is no relation between the water and haemoglobin concentrations.***

Melanin is the pigment that is the main absorber in skin, hair and iris in the eye. It is synthesized inside the melanocyte cells by the organelle melanosome.[14] The amount of melanin inside the melanosomes may vary, which is why people from different parts of the world have different skin colour. It is not possible to extract pure melanin from the melanosomes, since it is not soluble, and even if it were its optical properties would be altered.[13] Therefore, absorption properties of melanosome are used instead of the ones of melanin. The absorption for melanosome is high in the UV-region and decays exponentially for longer wavelengths according to the approximated empirical relation

$$\mu_a = 1.70 \cdot 10^{12} \lambda^{-3.48} cm^{-1}, \tag{5}$$

presented by Jacques and McAuliffe[15], where λ is in nm. This equation holds for melanosome in the skin.

2.3 Scattering

Scattering can be either elastic or inelastic. Inelastic scattering changes the energy of the scattered photon in contrast to the elastic scattering where the photon energy is preserved. If the scattering particles are small in comparison to the wavelength of the scattered light, the process is called *Rayleigh* scattering.[16, 7] Rayleigh scattering is proportional to the reciprocal of the wavelength to the power of four, λ^{-4}. This scattering process can, in a relativistic fashion, be illustrated as excitation to a virtual energy level followed by immediate relaxation to the ground state.

There is a small probability that the relaxation will leave the molecule in a higher vibrational state, i.e. with more energy, than it originally was in. Thus, the scattered light will have a longer wavelength than the incident. This wavelength shift, called the *Stokes* line, is the first component of Raman scattering and is well defined in relation to the wavelength of the Rayleigh scattered light. However, the strength of this side band is only approximately 10^{-3} times the strength of the Rayleigh line.[16] The second component of the Raman scattering is called the *Anti-Stokes* line. This involves a shift towards shorter wavelengths analogous to the one for the Stokes line. Here, however, the molecule is not in the lowest vibrational level before excitation and the relaxation ends in a lower

vibrational level in the ground state. Since the number density of molecules decrease for higher vibrational levels, the Anti-Stokes line is even weaker than the Stokes line is.

The third kind of scattering is the so called Mie scattering. This is due to scattering interactions with particles of comparable size to the wavelength of the light and depends approximately on the wavelength as λ^{-2}.[16] Rayleigh theory can be considered as a simplification of the more complex Mie theory, in the case of small scatterers. Both Mie and Rayleigh scattering are elastic processes, while Raman scattering is inelastic.

2.3.1 Scattering coefficient and anisotropy factor

Analogous to the absorption coefficient, the scattering coefficient, denoted μ_s [cm^{-1}], is associated with the light attenuation due to scattering in turbid media. It should be interpreted the same was as the absorption coefficient, i.e. as the probability of one scattering event per unit length.[10] Similarly the inverse of μ_s represents the scattering mean free path length. Due to the anisotropy of the light scattering in tissue, a parameter that measures the asymmetry of the scattering is introduced. This anisotropy factor, g, is defined as the average cosine of the deflection angle at a single scattering event.[10] The g-factor can take values from -1 to 1 where the minus sign indicates backward scattering. A g-value equal to -1 corresponds to total backward scattering and when g equals 1 the scattering is directed forward. If the g-factor is zero, equally much light will be scattered in the forward as in the backward direction. The medium is, in this case, most probably isotropically scattering, i.e. the scattering is symmetric and light is scattered in all directions with equal probability.[9]

The angular probability that a photon will be scattered from the direction $\boldsymbol{s}'$ to the direction $\boldsymbol{s}$ is given by a scattering phase function, signified $p(\boldsymbol{s}, \boldsymbol{s}')$. The alternative notation $p(\cos\theta)$ indicates that the light is scattered a specific angle θ between the $\boldsymbol{s}'$- and $\boldsymbol{s}$-directions. A frequently used phase function in tissue optics is the Henyey-Greenstein function, which was initially derived for diffuse radiation in a galaxy:[17]

$$p_{HG}(\cos\theta) = \frac{\left(1-g^2\right)}{4\pi\left(1+g^2-2g\cos(\theta)\right)^{3/2}}, \quad |g| \le 1. \tag{6}$$

As will be seen later, other approximations for the scattering phase function are currently used in tissue optics.

Combining the scattering coefficient and the anisotropy factor the reduced scattering coefficient is defined as

$$\mu_s' \equiv (1-g)\mu_s .^{10} \tag{7}$$

Using this parameter the anisotropic scattering from several scattering events, i.e. $(1\text{-}g)^{-1}$, with short path lengths are combined and approximated with one isotropic scattering event with long path length. The reduced scattering coefficient is a useful parameter since it is often difficult to extract values for both μ_s and g in a tissue sample using the common measurement methods. It is, however, important to keep in mind that this isotropy approximation is only valid when the total path length is long. For simulations involving short path lengths the g- and μ_s-values must be used.

2.3.2 Scattering in human tissue

In human tissue the scattering is due to variations of refractive indices. First consider tissue and organs as built up from layers of homogeneous media with different refractive

indices. Scattering, in this case determined by using the Fresnel equations from ***Section 2.1***, is the macroscopic average scattering. From this the refractive indices of different tissue types can be approximated. For most types of tissue, except adipose tissue, which has a refractive index of 1.46, the refraction index is in the 1.38 - 1.41 range at 633 nm.[18, 19] However, at small to intermediate incidence angles, the Fresnel scattering in the organ surfaces is quite small and has low significance. If, on the other hand, repeated structures or adjacent tissue layers are considered the total effect can be quite large.[20]

The scattering from finer structures can be studied by seeing the individual cells as homogeneous particles. The differences in refractive indices of such cells and the extracellular fluid are small. In fact, the ratio of the indices is close to unity resulting in a low degree of scattering.[20] However, due to the large number of cells, the scattering can be significant.

Finally the microscopic features of the cells will be considered. There are four main candidates that may contribute to light scattering. These are the cell membranes, the nucleus, the organelles and small structures within the organelles. Studies have shown that the cell membrane and the nucleus are the main contributors to the effective refractive index.[21] However, since other parameters such as structure, size and concentration affect the scattering, cell membrane and nucleus are not the dominating scatterers in tissue. Studies also shows that the cell membranes are responsible for scattering at small angles and that scattering at slightly larger angles are due to interaction with the nucleus. Light interaction with the organelles, including mitochondria, and the structures within them result in scattering at large angles.[22] The correlation between scattering efficiency and mitochondrial content has been found to be high. A highly inhomogeneous internal structure of a scattering object also increases scattering at large angles while the scattering in small angles are decreased.

In this section it has been concluded that the light scattering by the cell membrane and nucleus is of low significance compared to the scattering of mitochondrial content despite the fact that the former elements are the main contributors to the effective refractive index. Next, mathematical models of light distribution will be introduced.

2.4 Light distribution - a mathematical approach

The distribution of light in turbid media can be described analytically by Maxwell's equations, which describe the light as electromagnetic waves. A problem with this, in tissue optics, is that there is no general solution available for the tissue-light interaction situation.[9] It is also incredibly complicated to set-up models for media of random dielectric fluctuations to imitate the natural behaviour of tissue structures.

Another, more commonly employed, approach is to treat light as particles, photons. Transport theory is such an approach. Though, the theory of photons does not take effects such as diffraction and interference into consideration.[7, 8] This is, however, no limiting problem, since the light is assumed to be multiply scattered and such effects can be neglected.

2.4.1 Light transport equation

The transport equation is a statistical approximation of the photon energy transport in turbid media.[9] Main advantages of this equation are the possibility to solve it both analytically and numerically. The transport equation is based on the principle of energy conservation and is given by[9]

$$\frac{1}{c}\frac{\partial L(\boldsymbol{r},\boldsymbol{s},t)}{\partial t} = -\boldsymbol{s}\cdot\nabla L(\boldsymbol{r},\boldsymbol{s},t) - (\mu_s + \mu_a)L(\boldsymbol{r},\boldsymbol{s},t) + \\ + \mu_s \int_{4\pi} p(\boldsymbol{s},\boldsymbol{s}')L(\boldsymbol{r},\boldsymbol{s}',t)d\omega' + S(\boldsymbol{r},\boldsymbol{s}',t) \quad (8)$$

In the equation, $\boldsymbol{r}$ represents an arbitrary point in space (where the tissue volume element dV is located) and $\boldsymbol{s}$ is the light propagation direction. Further, $\boldsymbol{s}'$ represents all other directions and $d\omega'$ all solid angles, while t is the time-variable. $L(\boldsymbol{r},\boldsymbol{s},t)$ [W·m^{-2}·sr^{-1}] is the radiance, i.e. the radiant power per unit area and unit solid angle in the direction $\boldsymbol{s}$ at the point $\boldsymbol{r}$. c [m/s] is simply the speed of light in the tissue, given by $c = c_0/n$. The equation yields that the left-hand side of the equation represents the change in the number of photons at the point $\boldsymbol{r}$, in the $\boldsymbol{s}$-direction at time t.

This, at first sight, complicated formula can be explained by referring to ***Figure 4***, which illustrates the photon propagation and interaction in an infinitesimal volume element of tissue.

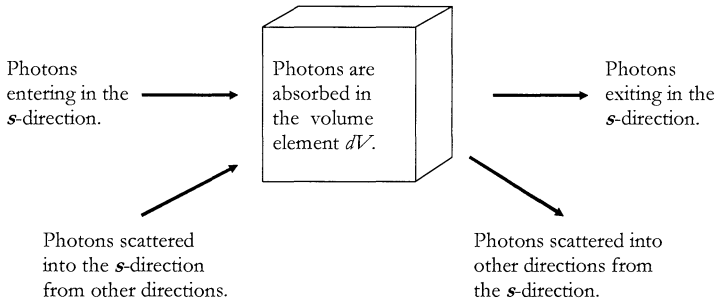

Figure 4: ***The different expressions in the light transport equation can be explained with this illustration. The light transport in one single direction, s, through an infinitesimal volume element dV is considered.***

The first and second terms on the right-hand side represent the photon losses in the system. The first term corresponds to escape losses through the boundaries and the second one is due to absorption inside the volume element and scattering to all other directions than $\boldsymbol{s}$. The third term is the gain through scattering from all other directions $\boldsymbol{s}'$ to the observed direction $\boldsymbol{s}$. The last term on the right-hand side is a source term for an arbitrary light source inside the volume element.

In the next section certain approximations will be made, reducing the transport equation to a diffusion equation, which is not as hard to solve analytically as the transport equation. In ***Section 2.4.3*** a method of simulating the photon transport in tissue, called Monte Carlo simulation, is described.

2.4.2 Diffusion approximation

Assuming spherical symmetry for the scattering particles, the light transport in tissue can be regarded as a diffusion process. The diffusion approximation equation received when expanding the light transport equation in spherical harmonics is

$$\frac{1}{c}\frac{\partial \phi(\boldsymbol{r},t)}{\partial t} = D\nabla^2\phi(\boldsymbol{r},t) - \mu_a\phi(\boldsymbol{r},t) + S(\boldsymbol{r},t).^{10} \quad (9)$$

The diffusion coefficient, D, originates from Fick's law[10] and is given by

$$D = \left(3(\mu_a + \mu_s')\right)^{-1}. \quad (10)$$

The approximation is valid only if the light distribution can be considered to be diffuse, why two requirements must be fulfilled. First of all the reduced scattering coefficient must be much larger than the absorption, i.e. $\mu_s' \gg \mu_a$. Second, the detector point $\boldsymbol{r}$ must not be too close to the source. As a rule of thumb, the light should be scattered at least ten times before detection.

For simple geometries, such as an infinite homogeneous medium, the diffusion equation can be solved analytically. Analytic solutions are also known for more complicated structures, e.g. for a semi-infinite homogenous medium, if certain boundary conditions are set up in combination with virtual dipole sources. If the medium cannot be regarded as homogenous, the diffusion equation must be solved numerically. Willem M. Star[9] has derived solutions to some important approximations of tissue structure.

2.4.3 Monte Carlo simulation

Monte Carlo simulations are based on a statistical model and simulate the photon path through turbid media using well-known probability functions for the path length and the scattering angle. Note that the total mean free path length equals the inverse total attenuation coefficient, i.e. $mfp_t = \mu_t^{-1} = (\mu_a+\mu_s)^{-1}$, with a typical value of about 100 μm for visible light.[23]

During a Monte Carlo simulation, each photon undergoes a series of events. A scheme illustrating the simulation process has been presented by Prahl et.al.[24] ***Figure 5*** shows a flow chart of such a scheme.

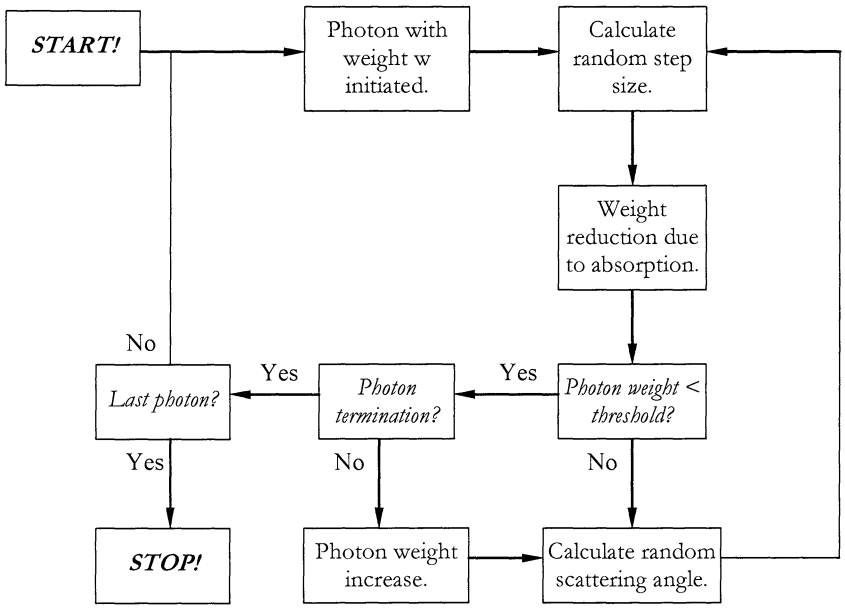

Figure 5: ***Flow chart illustrating Monte Carlo simulation as presented by Prahl et.al.[24]***

Each photon initiated in the process is assigned a weight, corresponding to the energy of the photon. For every movement with statistically determined interaction path length, this weight is reduced due to the absorption. It is also decreased if some of the photon's energy is transmitted through a tissue boundary. The latter occurrence is, however, not included in the flow chart in ***Figure 5***. If the photon weight exceeds some threshold value, a scattering angle will be estimated based on the phase function of the specific type

of tissue and the photon will be moved again. On the other hand, if the photon weight is below the threshold value it will either be terminated or gain new energy, i.e. the weight will be increased. This step is implemented to maintain the principle of energy conservation.[24] If the weight is increased, the photon will be scattered and once again start over from the part where the interaction path length is calculated. The process is repeated for as many photons as the user wants the algorithm to simulate. During the simulation the absorption and scattering is registered and post-calculations yield information about e.g. the fluence rate.

In many cases it is advantageous to use Monte Carlo simulations since these are not limited to simple geometries. Boundary conditions and inhomogenities do not result in impediments to the calculations. However, it will take a great deal of photons to achieve trustworthy statistics.

3 BLOOD AND ITS OPTICAL PROPERTIES

3.1 The anatomy and physiology of whole blood

Blood is one of the three components of the cardiovascular system (the other two are the heart and the blood vessels). The science concerned with the study of blood, blood forming tissue and the disorders associated with them is called haematology. Blood has three main functions.[14] First of all it is a *transporter* of oxygen from the lungs to the cells and of carbon dioxide in the opposite direction. It also carries nutrients, heat, waste products and hormones. Second, blood is used to *regulate* pH and body temperature. Its osmotic pressure also regulates the water content of the cells. The third task is *protection* against foreign microbes and toxins.

Blood is slightly alkaline with pH ranging from 7.35 to 7.45, and has a normal temperature of about 38°C. An average-sized adult has a blood volume of about 5 litres, which constitute approximately 8% of the total body weight. Blood or whole blood, as it is also referred to, is composed of the plasma and the formed elements (i.e. erythrocytes, leukocytes and thrombocytes) to an extent of 55% and 45%, respectively, see ***Figure 6.*** Further, 99% of the formed elements are erythrocytes. The ratio of the volume of blood cells to the volume of blood is physiologically important and is called haematocrit. In the following sections the anatomy and physiology of the different components of whole blood will be discussed briefly. For a deeper analysis and discussion, refer to literature as *Principles of anatomy and physiology*[14] and *Functions of the human body*[25].

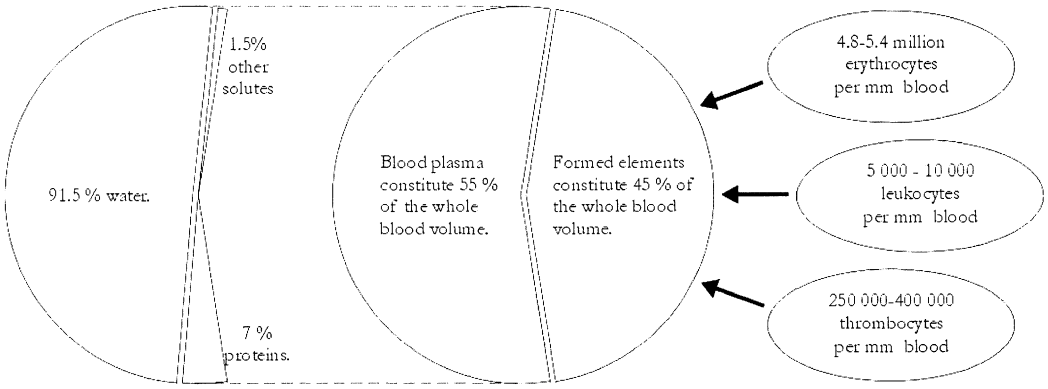

Figure 6: ***Whole blood is a complex composition of water solutes and formed elements.***

3.1.1 Blood plasma

Blood plasma is a slightly yellow liquid that consists of 91.5% water, 7% proteins and 1.5% of other solutes, mainly electrolytes such as sodium, potassium, calcium, phosphate, chloride and bicarbonate ions. Blood plasma is one of the three main extracellular fluids, i.e. the fluids outside the cells; the other two are lymph and interstitial fluid. Chemically these fluids are composed in similar ways. Though, blood plasma differs from the others by containing a larger number of leukocytes and considerably more protein.[14] The reason for this is that the large proteins are unable to diffuse through the endothelial cells of the vessel wall of the capillaries. Smaller molecules, however, can penetrate through the capillary walls. This type of diffusion is called osmosis and is a key factor in the transport of materials to and from the cells. The blood transports oxygen from the lungs, nutrients from the gastrointestinal tract and hormones from the

endocrine glands to the capillaries and further to the cells in the different organs. From the capillaries these substances diffuse into the interstitial fluid, which acts as a middle hand between the blood and the cells. In exchange, the blood receives carbon dioxide, which is carried to the lungs, and metabolic waste products, which are transported to the kidneys, the liver or the sweat glands to be excreted from the body.

3.1.2 Erythrocytes

The erythrocytes, also called red blood cells (RBC), are the oxygen carrying cells in the blood. The concentration of RBCs is controlled by negative feedback and is kept stable at about 5 million cells per mm^3 blood, se ***Figure 6***. The cell production is stimulated by tissue oxygenation, i.e. if a person is exposed to thin air or performs continuous exercise, the cell production is increased.[25] Each RBC contains approximately 280 million haemoglobin molecules. The globin protein in each molecule is composed of four polypeptide chains. To each chain a non-protein pigment called haeme is bound. The haeme pigment causes the red colour of the blood. Binding of the oxygen is due to the single iron ion (Fe^{2+}) located in the centre of each haeme molecule.

The RBCs lack nucleus and other organelles which makes them unable to reproduce by cell division. Instead RBCs are, as all other formed elements, developed by a process called hemopoiesis. The cells are here produced from stem cells in the red bone marrow. Red bon marrow exists only in a few different types of bone in the body. An erythrocyte is approximately 8-10 μm in diameter and the lack of nucleus contributes to the biconcave shape of its surface. This shape increases the surface which leads to an increased diffusion of oxygen into the cell. Another advantage of the biconcave cells shape is that their flexibility is increased. In this way they are able to squeeze trough small capillaries, some of which are as narrow as 3μm in diameter. However, the wear and tear of the cells affect their lifetime in a negative way. A normal lifetime of an erythrocyte is about 120 days. As a result, the fabulous amount of 2 million cells must be produced every second.

3.1.3 Leukocytes

The leukocytes, also referred to as white blood cells (WBC), have a number of tasks to carry out. Some of them kill microbes invading the tissue and causing illness by immune response, others clean up cellular debris and microbes following an infection. Another important function is excretion of enzymes that prevent histamine and inflammation in allergic reactions. There are several different kinds of leukocytes. These are highly specialized and different cell types are activated to take action in different situations. All leukocytes differ from the erythrocytes by having a nucleus. They are divided into two groups, the granulocytes and the agranulocytes. The granulocytes have conspicuous granules in the cytoplasm of the cells. The eosinophils, basophils and neutrophils that have diameters ranging from 8 to 12μm belong to this group. The agranulocytes have diameters in the range of 6-20μm and lack granules in the cytoplasm. This group is composed of monocytes and lymphocytes.

By *emigration* through the vessel walls the WBCs are able to interact with infected tissue far away from the vessels. The emigration process involves slowing down the cells and rolling them along the endothelium. Finally they stop and squeeze through the endothelial cells of the vessel walls. If a granulocyte or a monocyte has left the blood stream it will never return. A lymphocyte, on the other hand, continually recirculates from blood to interstitial space to lymphatic fluid and back to blood.

The individual functions of the different leukocytes are of no importance to this project. Only the functions of the lymphocytes, i.e. the B cells, the T cells and the natural killer cells, will be mentioned. These are the major combatants in defensive immune

responses. The B cells develop into plasma cells, which secrete antibodies. These antibodies neutralize, inhibit or destroy antigens that are invading the tissue by forming antigen-antibody complex. The T cells attack viruses, fungi, transplanted organs and cancer cells. Finally the natural killer cells attack a wide variety of infectious microbes and certain spontaneously arising tumour cells.

As shown in ***Figure 6***, the concentration of leukocytes in whole blood is 5 000-10 000 cells per mm^3 blood. A normal distribution of the different types of leukocytes is 60-70% neutrophils, 20-25% lymphocytes, 3-8% monocytes, 2-4% eosinophils and 0.5-1% basophils, respectively. Deviations from these percentages may indicate if a person suffers from a special illness.

3.1.4 Thrombocytes

The stem cells in the red bone marrow can also by influence of an enzyme called thrombopoietin develop into thrombocytes, or platelets. Each stem cell can be transformed to 2 000-3 000 platelets, which are disc-shaped and have a diameter of 2-4 μm. There are between 250 000 and 400 000 platelets per mm^3 whole blood, see ***Figure 6***. The platelets help stopping blood loss from a damaged vessel by forming so called platelet plugs. In this process the chemicals contained in the cytoplasmic granules contribute to make the platelets stick to each other and form the plug. These chemicals also promote blood clotting. For further information on thrombocytes and hemostasis (the process of stopping bleedings) please refer to the literature.[14]

3.2 The optical properties of blood

A fundamental understanding of the light absorption and scattering properties of tissue is essential in all diagnostic and therapeutic applications in medicine using laser light in order to optimize the result. The macroscopic properties, measured as μ_a, μ_s and g, yield information about the average absorption and scattering as well as scattering angle. These values can, with great advantage, be used in many applications and computations. It is, however, desirable to understand tissue-light interaction on a microscopic level. In order to increase the understanding about this, it has become quite popular to make studies with blood, since the RBCs' morphological properties change collectively.[26] Due to the changed morphology induced by a changed flow rate of the blood, it is possible to control these collective properties. Most tissues differ from blood in this matter, since they consist of more or less randomly oriented cells with various size and shape. Light scattering in tissue is mostly caused by the mitochondrial content, see ***Section 2.3.2***. Also the cell membrane and nucleus have some, though rather limited, influence on the scattering. Since the RBCs lack both organelles and nucleus it is likely that the main scattering elements in blood are the membranes of the red blood cells. This theory is confirmed by studies that have shown that the scattering is due to objects of comparable size to the RBCs.[27, 28] In such studies Mie theory computation is a commonly used mathematical method to model the red blood cells. Despite the differences of the actual cell shape and of that in the model, where each cell is approximated with a homogeneous sphere, the theoretical results have shown good agreement with experimental results. Studies have shown that this is due to that a Mie equivalent average radius of the RBCs can be derived.[28]

In order to treat light scattering of whole blood theoretically a great number of studies have been performed. The propriety of the normally used Henyey-Greenstein phase function has been questioned in connection to computations concerning blood due to the highly anisotropic scattering characteristics. Other phase functions have shown better

compatibility with experimental results, e.g. the Gegenbauer kernel and the Mie phase function.[29, 30]

Many different studies have shown that the absorption and scattering properties of blood is changed as a result of changes in the physiological properties of blood. Roggan *et al.*[31], e.g., have studied how the optical properties vary with respect to haematocrit, osmolarity, haemolysis and oxygen saturation.

Another factor that influences the optical properties is the heat induced during laser diagnostic and treatment modalities. Nilsson *et al.*[32] have looked into this matter. They concluded that there exists a critical temperature at approximately 45-46°C for blood. At this temperature a slight but very distinct change in the optical properties was observed. The g-factor decreased while both scattering and absorption coefficients increased. They also discovered that once the blood temperature exceeds the critical temperature, the changes in optical properties were irreversible. The results are suggested to be due to a shape transformation of the RBCs. At a temperature close below the critical temperature the cells take on a spherical form instead of their normal disc shape, a phenomenon called sphering.

Finally, some aspects of morphological properties will be discussed. Morphology involves qualities as e.g. cell shape, size, orientation, distribution and aggregate formation. In general, particles with considerable aspherical shape, exhibit strong asymmetric scattering, resulting in e.g. an elliptical angular scattering distribution while perfectly spherical particles yields isotropic scattering. Nilsson *et al.*[33] have used T-matrix computations to study the influence of cell shape on the angular distribution of scattering. The group concluded that the forward scattering was highly affected both by the three-dimensional shape and the optical thickness apparent to the incident light. The back scattering on the other hand was influenced only by the shape of the surface facing the incident beam. They found that sphering as well as elongation of a disc shaped RBC, which e.g. occurs physiologically when the cells experience an increased shear stress due to the flow rate of the blood, result in a decreased *g*-factor.

In another study, Enejder *et al.*[26] have investigated how the optical properties of whole blood flowing in a cuvette vary with flow speed and collective properties. Properties such as orientation, distribution and aggregate formation, is also referred to as secondary cell morphology while primary cell morphology refers to shape and size of individual cells. The degree of alignment and orientation is correlated with the flow speed of the blood. Thus, for low flow speeds the red blood cells are randomly oriented and for high flow speeds a higher degree of organization is received due to cell alignment and elongation. Also when blood is kept stationary the degree on organization is increased due to that the RBCs form aggregates. The studies showed that the scattering properties are significantly higher for blood with randomly oriented cells, i.e. for blood with low flow speeds, than for blood with a high degree of alignment and orientation, i.e. for stationary blood or blood with high flow speeds. The same tendency was found for the absorption properties. These results also indicated that the scattering properties mainly depend on secondary cell morphology while the absorption properties vary due to changes in the primary cell morphology.

In the literature it is hard to find concise information on the optical properties, probably because they depend on all the physiological parameters. Since no mathematical simulations of light-tissue interaction was made during this project, no hard effort was made to find exact values of the scattering and absorption coefficients and the anisotropy factor. However, it can be concluded that the anisotropy factor has a value of approximately 0.99 which means that the scattering is highly forward directed. For the absorption spectra of haemoglobin, refer to ***Figure 3***.

4 PRINCIPLE OF MICROSCOPY

Since Zacharias Janssen[34] invented the microscope in the late sixteenth century the development of such instruments have reached far. The microscopes of today are extremely complex regarding both optics and electronics. Until the late 1980s most microscopes had a fixed so called mechanical tube length which is defined as "the distance from the nosepiece opening, where the objective is mounted, to the top edge of the observation tubes where the eyepieces are inserted"[35]. Nowadays, however, most microscopes utilise infinity-corrected optics, which makes it possible to insert accessories such as prisms, polarizers and retardation plates etc. without introducing further optical aberration into the system.

In this chapter the image formation in conventional microscopes will be discussed followed by sections about microscope objectives and illumination systems. The chapter is finished with a description of optically sectioning, which can be achieved with confocal microscopy and by modifying the illumination system of a conventional microscope.

4.1 Image formation

Microscopes are based on the magnifying ability of a single lens or a lens system. An object placed at a distance z from the front focal plane of such a lens is imaged at a distance z' from the lens' back focal plane according to the left part of ***Figure 7*** with a well-defined magnification. Distances denoted s and s' are given as $z+f.f.l.$ and $z'+b.f.l.$, where *f.f.l.* and *b.f.l.* are abbreviations of front focal length and back focal length, respectively. It is possible to show that the intermediate image has a height $h'=h \cdot s'/s$, through simple geometrical relations. The lateral or transverse magnification is therefore given by s'/s.[8] The intermediate image is located at the aperture diaphragm of the eyepiece, which contributes to further magnification of the image onto the retina.

If an infinity-corrected microscope is used, the object is placed at the front focal plane of the objective, as shown in the right part of ***Figure 7***. Imaging of an extended object thus results in parallel light beams leaving the objective in several azimuths. These parallel light beams are focused by the *tube lens* and an intermediate image is formed at its back focal plane. In this case, the magnification from object plane to intermediate image plane is $h'/h=f'/f$, where f' and f are the focal lengths of the tube lens and the objective, respectively. The region between the objective and tube lenses pays an important role and is called *infinity space*. Since the light beams in the different azimuths are parallel, inserting different optical accessories, as mentioned above, does not to introduce further aberrations into system. This is due to that every light ray contributing to one single point in the image has travelled the same distance through the accessory.[36] One reason why infinity-corrected systems are of great importance is that such accessories are the key components in many contrast enhancing techniques.

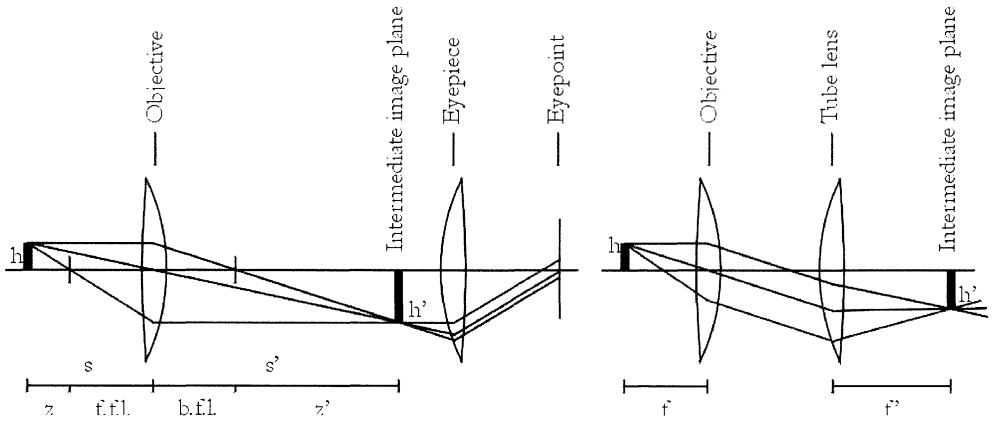

Figure 7: ***Microscope ray paths illustrating image formation in optical microscopes with finite tube length (to the left) and infinity-corrected systems (to the right).***

4.1.1 Point spread function

When a single point source is imaged by a lens, assuming the source to have a size smaller than the lens is able to resolve, the image of the source will be spread out due to diffraction and aberrations. The same happens when imaging an object; the conjugate image point to each object point is spread out by the *point spread function* (*psf*),[8] which is a function of the coordinates in the object plane and in the image point. The point spread function corresponds to the term *impulse response* in mathematics.[37] Thus, the point spread function is a measure of the imaging performance of an optical system. In fact it is related to both the optical transfer function and the modulation transfer function, which are two other well-known concepts indicating optical imaging performance.[8]

If the optical system can be regarded as aberration-free, the *psf* have the form of an Airy pattern. The Airy pattern is caused by diffraction due to the limited diameter of the lens.[8] Due to that the waves interfere near the image plane and produce a three-dimensional Fraunhofer diffraction pattern, the lens cannot focus the light waves to an infinitely small point. The intensity distribution of such pattern can be mathematically described by a Bessel function at the image plane.[8] The region enclosed by the first minimum of the Airy pattern defines the Airy disk. These have great importance to resolution of optical systems.

4.1.2 Resolution

Lord Rayleigh's criterion for resolution is often employed in microscopy. This criterion says that two adjacent point sources, such as the one in the previous section, are just resolved when the separation of the centres of the two Airy disks is larger than or equal to the angular radius of the Airy disk.[8] In the limit case the principal maximum of one pattern coincide with the first minimum of the other.[7] From the theory of Bessel functions the limit of resolution can therefore be represented by

$$\Delta x_{\min} = \frac{1.22 \cdot \lambda}{2 \cdot \text{N.A.}} = \frac{0.61 \cdot \lambda}{\text{N.A.}}, \quad {}^{38,39} \tag{11}$$

where $\Delta x_{\min}$ is the minimum separation of two just resolvable objects, λ the light wavelength and N.A. the numerical aperture of the lens.

In microscopy, resolution is defined as the smallest distance between two points on a specimen that can be distinguished as two separate entities. Lord Rayleigh's criterion,

though, is only one of several equations that have been derived to give an expression for the resolution.[38] None of these should, however, be considered as any absolute physical laws. Though, it is obvious in ***Equation 11*** that the resolution is related to the wavelength of the light used to illuminate the specimen and the numerical aperture of the system. In general a short wavelength yields better resolution than do longer wavelengths. Objectives are, however, corrected optically for specific wavelengths, as described in ***Section 4.2***. Thus, using too short wavelengths will degrade the image quality.

When it comes to the numerical aperture it is possible to resolve finer details the higher the *numerical aperture* of the system. Since the eyepiece does not contribute to the resolving power of the microscope, but merely magnifies the details in the intermediate image,[40] it is the objective that is primarily responsible for the resolving power of a microscope. The concept numerical aperture will de discussed more thoroughly in the section about microscope objectives.

So far we have only discussed the lateral resolution, which is measured perpendicular to the optical axis. The axial resolution, measured parallel to the optical axis, is referred to as *depth of field*. The distance from the nearest to the farthest planes in the object simultaneously in focus defines the depth of field, which is determined only by the numerical aperture of the objective.[40] The term is often confused with *depth of focus*, which refers to the focal depth of the image.

Other factors that affect the resolution are optical alignment and numerical aperture of the substage condenser.[38] To ensure maximum resolution it is of great importance that the optical components are properly aligned. The aperture diaphragm of the substage condenser also has to be adjusted so that the light cone is matched correctly to the numerical aperture of the objective.

4.1.3 Contrast and noise

In conventional bright-field microscopy, many objects are visible and others are transparent. The visible objects are referred to as *amplitude objects*, since they change the intensity of the transmitted or the reflected light. These intensity changes can occur due to spatial differences in absorption and reflection in an object. Naturally coloured and artificially stained objects also belong to the group of amplitude objects. The transparent objects, comprising e.g. many living cells and their organelles, do not alter the intensity the way amplitude objects do. However, they introduce a phase shift of the light and are therefore called *phase objects*.[41] The phase shift is caused mainly by refraction index and thickness variations in the object. These variations introduce differences in optical path expressed as $(n_s - n_o) \cdot d$, where d is the thickness of the specimen and n_s and n_o are the refractive indices of the surrounding medium and the specimen, respectively. A phase object can be phase-retarding or phase-advancing depending on weather its refraction index is grater than or lower than that of the surrounding medium, respectively.[41]

Optical contrast is another important concept in microscopic imaging. While resolution is a concept that is possible to describe, measure and manipulate, contrast is a more abstract concept. It reflects the noisy reality and is a limiting factor in the ability to use the resolution available in an optical system. Contrast depend upon properties such as absorption, reflection, scattering and spatial variations in refractive indices of the specimen. The most usually type of contrast referred to is brightness contrast that arises due to brightness differences between the object and the surrounding medium resulting in interference of the monochromatic illumination. [41] Under some circumstances this also applies for white light illumination.[41] Brightness contrast can be defined mathematically in various ways, e.g. as the relative intensity

$$C = \frac{n_b - n_d}{n_b + n_d} = \frac{n_b - n_d}{2 \cdot n_{avg}},^{39,41} \tag{12}$$

where n_b and n_d are the intensity of the bright and dim portions, respectively, and n_{avg} is the average intensity. If stray light, n_{stray}, is accounted for, ***Equation 12*** will be extended to

$$C = \frac{n_b - n_d}{\sqrt{n_b^2 + n_d^2 + 2 \cdot n_{stray}^2}}. \tag{13}$$

Stray light, or background light, is additive light that does not contribute to the image information. Such light is equally intense from every nearby object point. Light from the bright and dim portions are now n_b+n_{stray} and n_d+n_{stray}, respectively.

Photon noise or *quantum noise* is the irreducible noise caused by the random arrival times of the photons to the detector. Such noise is proportional to the square root of the number of photons falling on each pixel during one integration time of a detector,

$$N \propto \sqrt{n_{avg}} \propto \sqrt[4]{n_b^2 + n_d^2 + 2 \cdot n_{stray}^2}. \tag{14}$$

Since the signal is proportional to the difference in intensity in the bright and dim portions, $S \propto n_b+n_{stray}-n_d-n_{stray} = n_b-n_d$, the signal-to-noise ratio is

$$SNR = \frac{S}{N} \propto \frac{n_b - n_d}{\sqrt[4]{n_b^2 + n_d^2 + 2 \cdot n_{stray}^2}} \propto C\sqrt{n_{avg}}.^{39} \tag{15}$$

Thus, visibility depends on both contrast and the illumination level. In order to achieve a good signal-to-noise ratio we want high contrast and great average intensity. In many cases the stray background light dominates the illumination. Then, the signal-to-noise ration becomes $SNR \propto 0.84 \cdot (n_b - n_d)/\sqrt{n_{stray}}$. It is obvious from this equation that it is important to reduce stray light to get better visibility.

Throughout the years many specialised techniques for contrast enhancing based on reduction of stray background light has been developed. Among these are e.g. dark field microscopy, phase contrast microscopy, polarized light microscopy, differential interference contrast microscopy and fluorescence microscopy. More information about these techniques can be found on the Molecular Expressions Microscopy Primer home page[36] or in the literature such as "Advanced light microscopy" by M. Pluta.[42] Another technique is confocal microscopy, which has had a major impact on biological and biomedical imaging. Confocal microscopy will be discussed in ***Section 4.4.1***.

4.2 Microscope objective lenses

The objective lens is the most vital part of the imaging system in a microscope. It is responsible for resolving details in the object and magnifying these to the intermediate image plane. Different situations require different degrees of magnification. To meet these requirements there are objective lenses available in a wide range of magnifying powers from a couple of times (low power objective lenses) to 100x and beyond (high power objective lenses). Objective lenses also differ with respect to correction for optical

aberrations and are thus classified into three groups.[43] *Achromatic objective lenses* are corrected for axial chromatic aberration in two wavelengths (red and blue) and for spherical aberration in a green wavelength (which is chosen since it is located in the centre of the visible wavelength range). In addition to the two wavelength axial chromatic correction at red and blue wavelengths, *fluorite objective lenses* are corrected for spherical aberrations for the same two wavelengths. Finally, *apochromatic objective lenses* are chromatically corrected for three wavelengths (red, green and blue) and spherically for two (red and blue). All three classes of objective lenses suffer from field curvature, which means that the image is not focused to a single plane. This imaging error can be overcome either by using a compensating eyepiece or by using flat-field corrected objective lenses. The latter are called *plan achromatic*, *plan fluorite* and *plan apochromatic objective lenses.*

As mentioned in the ***Section 4.1.2*** the numerical aperture of an objective lens is critical to the resolving power of a microscope. Numerical aperture, abbreviated N.A., is a measure of the light gathering ability and the resolution. For a single lens it is given by the ratio of its diameter and focal length.[7] An alternative definition can be derived by referring to the cone of light which is accepted by the lens' aperture, se ***Figure 8***.

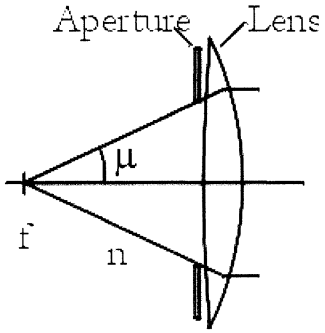

Figure 8: ***The numerical aperture is defined by the focal length and the aperture of the lens.***

With n as the refraction index of the imaging medium between the specimen and the front lens of the objective lens and μ as half the angular aperture the numerical aperture is defined as

$$\text{N.A.} = n \cdot \sin \mu . \qquad \textbf{(16)}$$

Since the sin-expression vary from zero to one it is obvious that the maximum theoretical value of the numerical aperture equals n. It is, however, difficult to achieve numerical apertures close to the theoretical maximum value. For "dry" objective lenses, e.g., where the imaging medium is air, $n = 1$ but it is hard to make such objective lenses with numerical apertures larger than 0.95.[38] Corrections for optical aberrations play an important role since they tend to increase with the numerical aperture. At a specific magnification, highly corrected objective lenses usually have much larger numerical aperture than do objective lenses with low degree of optical correction.[36, 38] In ***Section 4.1.2*** we concluded that an increase in numerical aperture improves resolution. In order to achieve numerical apertures greater than 1.0, immersion objective lenses have to be used. If such an objective is used an immersion medium fills the volume between the objective lens and the cover glass at the object. This results in that the light is refracted in smaller angles at the surface between the cover glass and the imaging medium.[44] Therefore more diffraction orders are focused by the objective lens and finer

details can be resolved. Popular immersion media are water, glycerine and immersion oil with refraction indices 1.33, 1.47 and 1.51 respectively.[38]

It is not only the lateral resolution that is affected by changes in numerical aperture of the objective lens. Depth of field, e.g., varies with magnification and numerical aperture and is, with constant magnification, also improved with increased numerical aperture.[40] The working distance of the objective lens, i.e. the distance from the front lens to the front focal plane, on the other hand is decreased when numerical aperture is increased.

4.3 Illumination

Accurate adjustment of the illumination system of a microscope is crucial to the quality of the image. The illumination system can be set-up for either transmitted or reflected illumination (sometimes they are used simultaneously). These two ways to achieve proper illumination can be realised in many ways. There are, however, several requirements an illumination system has to met.[36, 45] First of all the light must be uniformly distributed over the specimen. Second, the illuminated area of the specimen must be no larger than the field of view, i.e. the area of the specimen which is imaged, in order to avoid disturbing reflections and refractions in oblique angles from the specimen and the various lens mounts. Glare generated this way has to be prohibited in order not to risk contrast reduction. Dust and imperfections at the surfaces of the condenser lens are also desired not to deteriorate the illumination. One advanced procedure for microscope illumination which meets all these requirements was presented in the early twentieth century in a publication by August Köhler. An English translation of the article can be found on the Molecular Expressions Microscopy Primer homepage.[45] Since this type of illumination was employed during this project, the rest of this section will be devoted to explain how Köhler illumination works.

4.3.1 Köhler illumination

The Köhler illumination technique can be realized as either a transmitted or a reflected light system. Correctly adjusted, it not only fulfils the requirements stated above, but also protects the specimen from overheating due to heat exchange with the light source.[45] The latter is achieved by using a collector lens of fairly large focal length. ***Figure 9*** provides a schematic illustration of the illumination and image-forming light paths in a microscope using transmitted Köhler illumination. When studying the illumination light path it is clear that the two light rays are focused at the light source, at the aperture diaphragm, at the objective back focal plane and at the eyepoint. These four planes constitute the *conjugate planes* in the path of the illuminating light rays.[36] Similarly, the conjugate planes of the image-forming light path are the field diaphragm, the specimen plane, the eyepiece field diaphragm and the retina of the eye located at the eyepoint (not shown in the illustration).

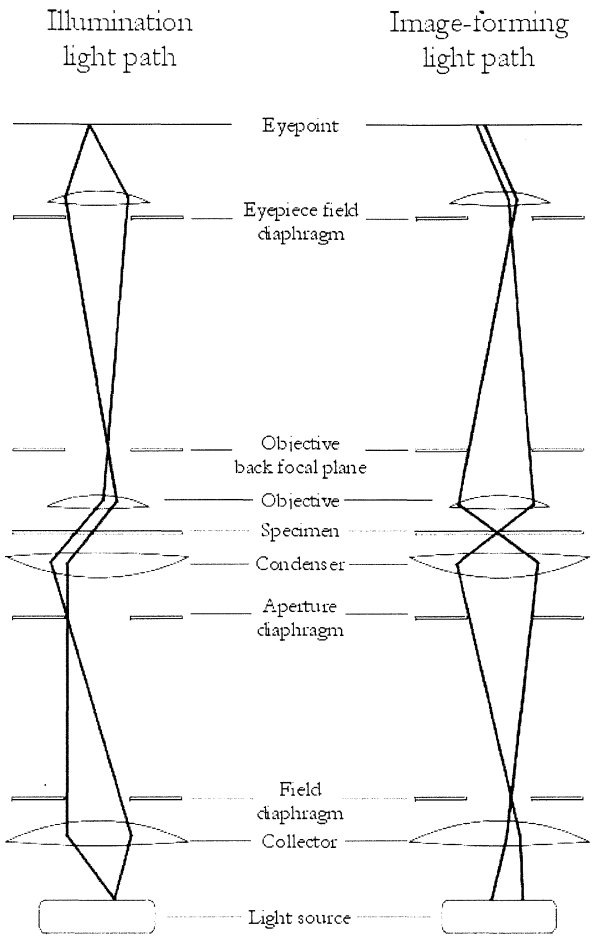

Figure 9: ***Schematic illustration of the illumination and image-forming light paths for transmitted Köhler illumination.***

Figure 9 illustrates how one single point on the light source contributes to the illumination of the entire field of view at the object plane and also how a large portion of the light source illuminates every single point at the object plane. The requirement of uniformly distributed illumination is therefore fulfilled. Due to the presence of the conjugate planes the field diaphragm, which is imaged onto the specimen, merely controls the area of illumination so that it is no larger than the field of view. Changing the field diaphragm does not affect resolution or numerical aperture, nor does it vary the light intensity. It does, however, if properly adjusted (i.e. opened to lie just outside the field of view) prevent contrast reduction due to glare. Finally, since the light source is not imaged at the object plane, the image is not deteriorated due to dust and imperfections at the condenser lens' surfaces.

In previous parts of this chapter the objective's numerical aperture and its significance to e.g. resolving power has been discussed. However, in order to take advantage of a microscope objective's full potential, the aperture diaphragm at the substage condenser lens has to be properly adjusted so that the light cone matches the numerical aperture of the objective.[38] Alignment of the substage condenser and adjustment of the condenser aperture diaphragm are in fact the most critical aspect to Köhler illumination.[36] A too narrow aperture diaphragm will introduce diffraction artefacts such as fringes or other pattern formations. If the aperture is too wide the image will suffer from glare resulting contrast reduction. It is extremely important not to use the aperture diaphragm to control illumination intensity or illumination errors as those mentioned will occur.

Instead, neutral density filters and adjustable power supplies for the light source should be used.[36]

The reflected light Köhler illumination system differs from the transmitted light system in one particular important way; the objective lens also serves as condenser. This means that the condenser is well-corrected for optical aberrations and that it is automatically aligned and positioned in relation to the objective. ***Figure 10*** illustrates the image-forming light path for Köhler illumination with reflected light. Note that in this specific case illustrated the objective is infinity-corrected. Notice further that the conjugate planes are the same as in a setup for transmitted light.

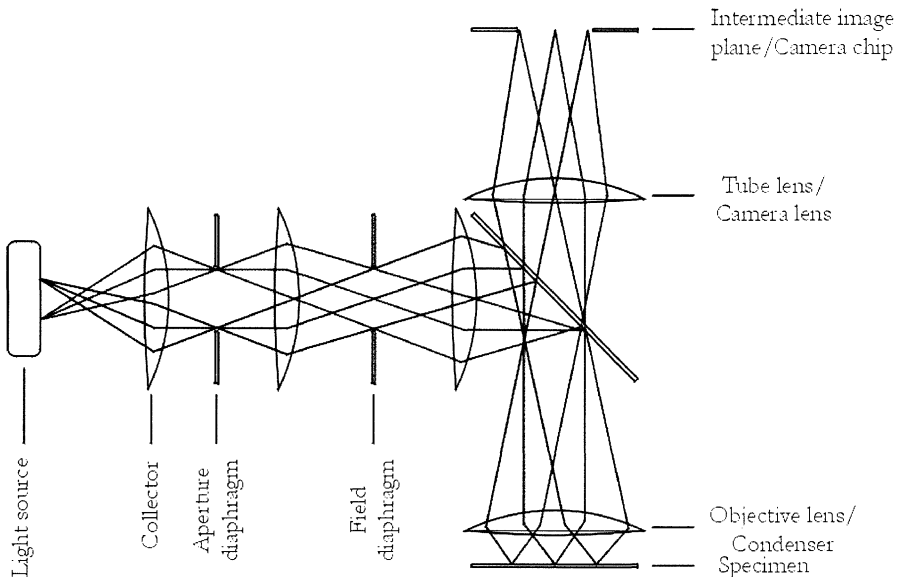

Figure 10: ***Schematic ray trace of the image-forming light path for reflected Köhler illumination.***

4.4 Optical sectioning microscopy

Previously in this chapter we have been introduced to image formation and other important factors in microscopy. The following sections will extend the understanding of microscopy to optical sectioning. Confocal microscopy, which is used extensively in biomedical applications, will be discussed followed by a description of how amplitude modulated light can be used to achieve similar results, i.e. depth discrimination.

4.4.1 Confocal microscopy

In ***Section 4.1.3*** it was concluded that reduction of stray background light improves the visibility in microscopy, due to an increased signal-to-noise ratio. The main advantage of confocal microscopy is, though the resolution is slightly better, the increased contrast (stray light reduction).[39] Even when the image point is buried deep in a thick sample, the contrast conditions are improved.

The foundation of confocal microscopy is that one single point in the specimen is imaged at a time, by reducing the light from every other point at that time. Thus, the price to pay for the improved contrast is that the specimen or the light has to be scanned in order to image the entire object. Scanning can be made both lateral and axial, which permits volume structures to be imaged in three dimensions. The principle of confocal microscopy can be understood by the following simple explanation.[39,46] Imagine two points at different depth in a specimen and only one of them on the optical axis, as in

Figure 11. The points are imaged by the objective at different image planes. If a pinhole is placed conjugate to the axial point the intensity of the image of the other point will be reduced. As a matter of fact this holds for light from just any other point. Finally a point source is placed conjugate to the axial point and the pinhole. This way only the axial point is intensely illuminated. The light source, object point and pinhole are confocal, hence the name confocal microscopy. Only an object volume confocal to the source and the pinhole contributes to the detected light. Even if a volume is illuminated but separated from the focused plane, the light it remits will miss the pinhole and is not detected.

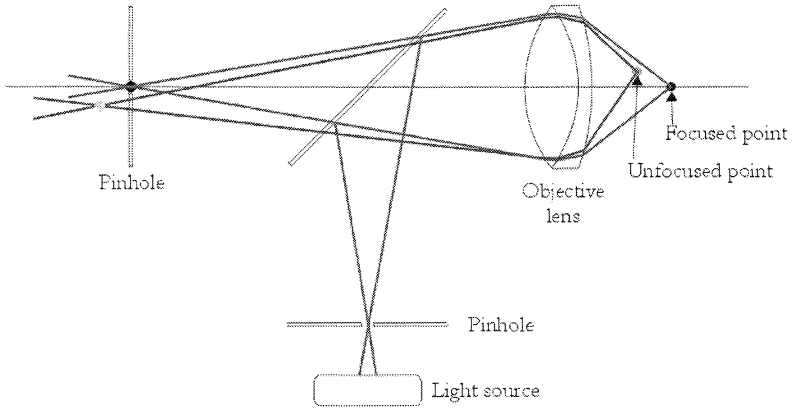

Figure 11: Illustration of the discrimination of unfocused points in confocal microscopy.

From ***Section 4.1.1*** we know that the image of the point source at the object is defined by the point spread function. If identical optics is used, as in reflected light microscopy, the same *psf* describes the observed object volume. Thus, the point spread function for a confocal microscope is the product of two identical functions, $psf_{confocal} = psf^2$.[39] The resolution, determined once again by applying the Rayleigh criterion, is then given by

$$\Delta x_{confocal} = \frac{0.44 \cdot \lambda}{\text{N.A.}}.^{39} \qquad (17)$$

Comparing with ***Equation 11***, it is obvious that the resolution is only slightly improved.

The contrast on the other hand is increased. This is due to a couple of reasons. First, the subsidiary peaks of the diffraction pattern described by the $psf_{confocal}$ are suppressed. This means that the energy is concentrated to the central peak. A bright peak near a dim one is therefore less likely to contribute to the background light of the dim peak, which can be seen as resolved. Another reason for the contrast improvement is the differences in interpretations of *psf* and $psf_{confocal}$. For the *psf* in conventional wide-field microscopy the energy is the same in every plane parallel to the focused plane. $psf_{confocal}$, however, represents only the portion of energy that has reached the focused plane in the object and then passed the pinhole. Consequently, the resolution is less degraded by contrast variations in confocal microscopy.

Naturally, a physical pinhole cannot be infinitely small. The larger the pinhole, the more photons will be detected, but also more stray light will be accepted and reach the detector. If a pinhole, either at the detector or the illumination side, is larger than the resolving ability of the objective, when imaged onto the object, a convolution of the pinhole with the *psf* is required before multiplication of the two functions. Such a convolution will smear the *pfs* over the pinhole's image. R.H. Webb[39] has shown that the confocal properties are well preserved as long as only one of the pinholes is large.

However, if both pinholes are large contrast is degraded towards levels as in the wide-field situation.

4.4.2 Modulated light to achieve confocal properties

The major drawback with confocal microscopy is the scanning time. It is desirable to be able to acquire confocal or optically sectioned images without the time consuming sequential illumination and acquisition of each object point. Various methods for obtaining three-dimensional information of an object have been proposed, based on the idea to project an illumination pattern on the object.[1] In a conventional microscope it is only the zero spatial frequency that does not attenuate with defocus. A microscope with a modified illumination system, that project a grid with a single spatial frequency onto the object, can be used to extract the information from the focal plane only. However, the grid will be superimposed on the image and the previously suggested methods lack any simple way to remove the pattern from the image.

M. A. A. Neil et. al.[1] have developed a method to achieve optical sectioning in a wide-field microscope that involves removing the superimposed grid pattern. They have placed a cosine-grating, of the form

$$S(t_0,\omega_0) = 1 + m\cdot\cos(\tilde{\nu}t_0 + \phi_0), \tag{18}$$

in a plane conjugate to the object plane in the microscope. The optical coordinates, t and ω, are related to real coordinates through $(t, \omega) = 2\pi\cdot\text{N.A.}\cdot(x,y)/\lambda$.[47] In ***Equation 18***, m and ϕ_0 denote the modulation depth and an arbitrary phase, respectively. $\tilde{\nu}$ is the normalized spatial frequency, which is defined through the actual spatial frequency ν and the magnification between the planes of the grating and the specimen β, as $\tilde{\nu} = \beta\lambda\nu/N.A.$ The normalized spatial frequency gives an indication about the sectioning strength of the system. $\tilde{\nu} = 0$ and $\tilde{\nu} = 1$ corresponds to minimum (as conventional microscopy) and maximum sectioning strength, respectively. The image intensity can now be written as

$$I(t,\omega) = I_0 + I_c\cos\phi_0 + I_s\sin\phi_0. \tag{19}$$

I_0 is the conventional microscope image, while I_c and I_s corresponds to the images due to cosine- and sine-modulations, respectively. The grid pattern can be removed by forming $I_{sec} = (I_c^2+I_s^2)^{1/2}$. This can be achieved by acquiring three images, I_1, I_2 and I_3, where the relative phase of the grating is $\phi_0 = 0$, $\phi_0 = 2\pi/3$ and $\phi_0 = 4\pi/3$. I_{sec} can now be calculated by

$$I_{\text{sec}} = \sqrt{(I_1-I_2)^2 + (I_1-I_3)^2 + (I_2-I_3)^2}\,. \tag{20}$$

The conventional microscope image I_{con} is calculated simply by adding the three images. Furthermore, Neil et. al.[1] have showed that the sectioning strength is given by

$$I_{\text{sec}} \propto \left| 2\frac{J_1(2u\tilde{\nu}(1-\tilde{\nu}/2))}{(2u\tilde{\nu}(1-\tilde{\nu}/2))} \right|, \tag{21}$$

where u is the normalized defocus parameter defined through the actual defocus z by $u = 8\pi \cdot z \sin^2(a/2)/\lambda$. This confirms that a microscope based on this principle exhibit optical sectioning in the same way as a confocal microscope.

Since first presented, the use of this method has reappeared in several publications. Wilson et. al.[48] have used it for real-time three-dimensional imaging. Cole et. al.[2,3] have used structured light in combination with fluorescence lifetime imaging. The three-dimensional imaging has been combined with fluorescence lifetime imaging and spectral resolution by Siegel et. al.,[4] Elson et. al.[5] and Webb et. al..[6] Ansari et. al.[49] have depth-resolved imaging with photorefractive holography. The method has been used by Lee et. al.[50] to construct a noninterferometric wide-field nanometer optical profilometer by also applying the principle of differential confocal imaging.

5 SYSTEM DESCRIPTION

In this chapter the entire system, shown in ***Figure 12***, and the parts that it is built up of will be described. Initially several opto-mechanical systems available on the market were considered. It was decided, however, that the physical design of the microscope was to be based on the *Microbench*-system from *Linos Photonics*.[i] This system has the advantage that the optics will be automatically aligned. Also the final microscope setup will be rather compact and easy to adjust. However, for some of the functions there were not parts available, at least not to a reasonable cost, to meet all out needs. Therefore, during the construction phase, some specially designed parts had to be constructed. These will be presented in more detail during the outline of this chapter and in the appendices. Furthermore, the chapter is divided into four sections. First the microscope objective lens will be described followed by descriptions of the illumination and imaging systems and, finally, the construction of the specimen mount. The reader is referred to the schematic illustration of the system in ***Figure 13*** during this system description.

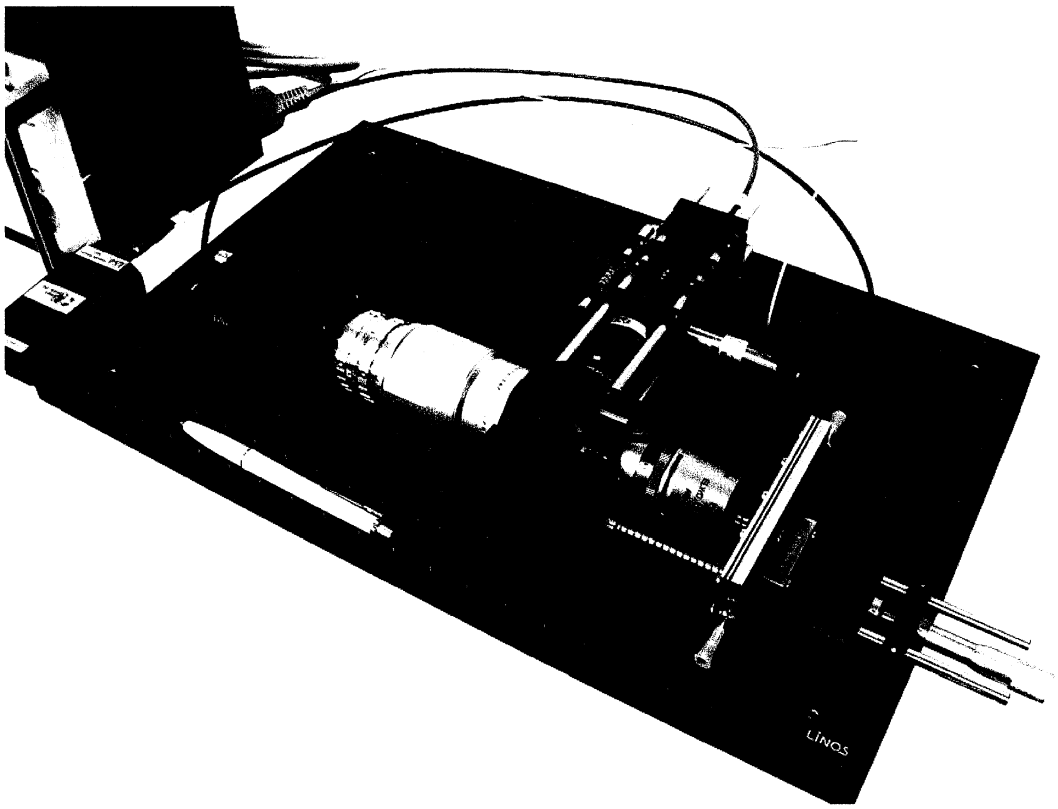

Figure 12: Photograph of the compact microscope constructed during this project.

[i] Linos Photonics can be found at http://www.linos-photonics.de/en/homefr1.html.The Swedish retailer is Azpect Photonics AB (at http://www.azpect.se).

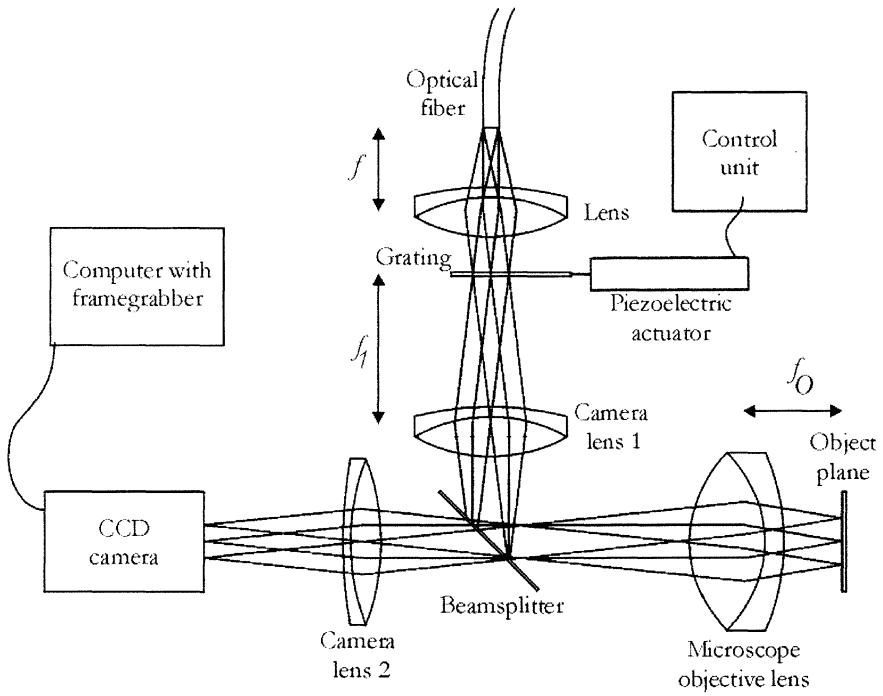

Figure 13: ***Schematic illustration of the microscope setup. Illumination and imaging can be separated as two different systems of the setup.***

5.1 Microscope objective lens

The objective used in the microscope is a 60x plan fluorite infinity-corrected "dry" objective lens manufactured by Nikon. This means, as described in ***Section 4.2***, that it is optically corrected for spherical and axial chromatic aberrations at two wavelengths. Also, the image does not suffer from field curvature and no immersion media (other than air) should be used. The objective's focal length is 3.3 mm, corresponding to the normally used 200 mm tube length divided by the magnification of the lens, and it has a numerical aperture of 0.70. The working distance of this Extra Long Working Distance objective is 2.1-1.5 mm. The back focal plane is located 50.4 mm from the shoulder of the thread.

The objective lens is mounted in the microscope by screwing it firmly into a modified *Mounting plate with mounting holes*, which is a standard component of the Microbench-system. A M25x0.75 thread is applied to the centre hole, matching the thread of the microscope objective.

5.2 Illumination

Illumination is, as has been said before, a critical part of a microscope. In this microscope, reflected Köhler illumination, described in ***Section 4.3.1***, is utilized. Our system, however, differ in one aspect. Since an optical fibre is used to lead the light into the microscope, there is no risk of overheating the specimen. Thus, no collector lens is needed and the fibre-tip is placed where the aperture diaphragm would be in conventional Köhler illumination, as shown in ***Figure 10***.

The fibre is centred in the optical system by an SMA-connector mounted in a specially designed adjusting housing, see ***Appendix A***. This device allows the fibre to be adjusted to the focal point of an achromat of focal length 20 mm.

The light then passes a cosine-modulated transmission grating, which is placed on a piezoelectric actuator. The amplitude grating, which is located at a plane conjugate to the

object plane, was produced on a photographic glass plate in a holographic setup, as described in ***Section 6.2***. The piezoelectric actuator, a Physik Instrumente[i] P-840.20 piezo, is connected to a control unit, designed by Åke Bergquist at the Electronic Workshop at the Division of Atomic Physics. The actuator, which is attached to the setup using the mounted described in ***Appendix B***, will translate the grating a distance corresponding to the voltage applied by the control unit. The maximum translation of the actuator is 30 μm and voltages ranging from 0 V to 100 V may be applied. In ***Section 4.4.2*** it was concluded that in order to achieve optical sectioning without a superimposed grid pattern, three images should be acquired. Thus, for imaging of stationary objects, three voltages have to be applied. To set the voltages, the set/run-switch, on the front panel of the control unit, first has to be switched to the set-position, see ***Figure 14***. Then the first and second trig-switches have to be switched on, individually, while the corresponding potentiometer is adjusted. To adjust the third potentiometer, both the first and second trig-switches have to be switched on. The trig-3-switch overrides the other two and activates the potentiometer below the display.

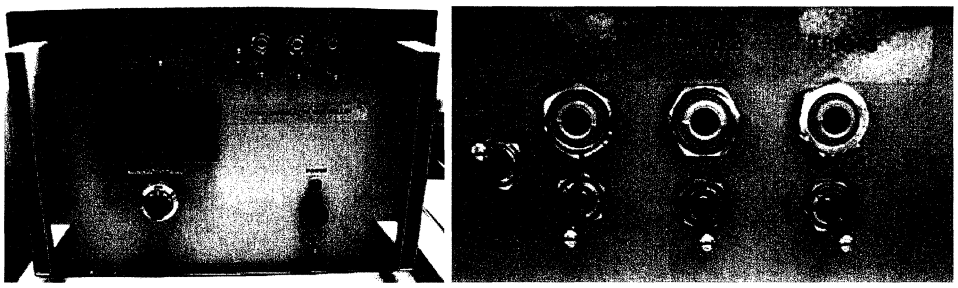

Figure 14: The control unit for the piezoelectric actuator.

After setting the voltages, the control unit can either be controlled manually, or, by switching the set/run-switch to the run-position, by the computer via the VHDCI-contact at the framegrabber card. When a voltage is applied to the actuator, a certain time passes before the grating reaches its desired position. When flowing red blood cells are studied, the images should be acquired within a very short period of time to prevent the image from being blurred due to the movement of the specimen. This suggests that all three images should be acquired during a rapid sweep of the grating.

The light passing the grating is refocused with camera lens 1, a Schneider-Kreuznach Xenoplan 2.8/50 mm lens.[ii] This lens is mounted in the system by its C-thread. The grating can be adjusted to the back focal point of the camera lens, located 17.51 mm behind the shoulder of the thread, by a micrometer construction.

Finally, the light is deflected into the back of the microscope objective lens by a beamsplitter plate, places in a *Beam-deflector cube 30* (a standard Microbench component). The cube is placed on a specially designed mounting block, see ***Appendix C***, to increase the stability of the system. The beamsplitter's dimensions are 20 mm x 30 mm x 2.5 mm, and for unpolarized light at an incidence angle of 45° reflectance ≈ transmittance ± 5%. Due to the 50 % light lost per pass in the beamsplitter, the maximum detectable light intensity is only one quarter of the initial light intensity, on condition that 100 % of the light reaching the specimen is reflected. (This corresponds to an attenuation of 6.0 dB in the system.) The light lost in the first reflection at the beamsplitter is captured by a beamdump, described in ***Appendix D***. This reduces the stray light in the system.

---

[i] Company homepage at http://www.physikinstrumente.de/

[ii] Datasheet found at http://www.schneideroptics.com/oem/c-mount/visible_spectrum/pdf/Xenoplan_28_50.pdf

5.3 Imaging

The light reflected and backscattered by the specimen is collected by the objective lens. The light is then refocused to a CCD camera chip by camera lens 2, which is a Schneider-Kreuznach Tele-Xenar 1:2.8/100 mm lens. The lens, and CCD, is attached directly to the beam-deflector cube with the help of a mounting ring screwed firmly to the filter-thread of the camera lens, see ***Appendix E***.

During the project, three different cameras were used. The first camera was an old Pulnix TM-860, with unsatisfactory image properties and rather poor signal-to-noise ratio.

The second camera was a scientific grade CCD, model LN/CCD-1024-EHRB/1, from Princeton Instruments, Inc., Princeton, NJ. The camera was cooled to -60 °C with liquid-nitrogen and controlled with a special computer software and a separate control unit. The major drawbacks with the Princeton-camera are the physical size of the camera and the control unit, the poor compatibility with the rest of the system (it is difficult to align the camera) and the long acquisition and readout times. However, the signal-to-noise ratio is very high due to the high sensitivity and suppression of the dark current, achieved by the cooling.

The last camera, a JAI[i] CV-M10 SX progressive scan CCIR camera, was bought[ii] to replace the poor quality Pulnix-camera. The JAI-camera has a ½" chip with pixels of the dimension 8.3 x 8.3 μm. The camera is connected to a National Instruments[iii] IMAQ NI PCI-1409 framegrabber card in a computer.

5.4 Specimen mount

The specimen is placed on a *Micrometer-driven translational stage*, a standard Microbench component, which enables the displacement of the object to the plane of focus. If a stationary object is studied, it can be placed on a *Mounting plate* attached to the translational stage. When studying flowing whole-blood, a cuvette is attached, by screwing it firmly, to the translational stage. The cuvette has been specially designed and constructed for the system. A photograph of the cuvette is shown in ***Figure 15*** and the drawings can be found in ***Appendix F***.

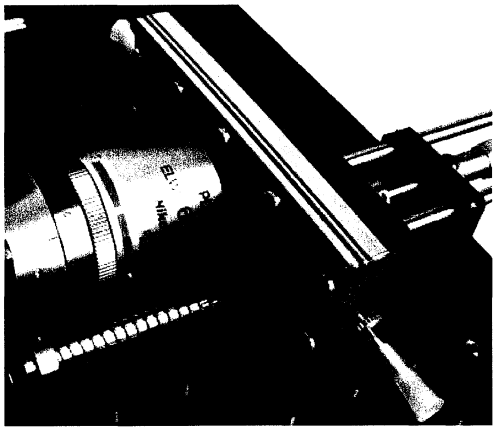

Figure 15: Photograph of the cuvette, which is designed for flowing blood.

[i] JAI's homepage is found at: http://www.jai.dk/.
[ii] Orbis, the Swedish retailer is found at http://www.orbis.se.
[iii] National Instruments' homepage is found at: http://www.ni.se.

6 SYSTEM PERFORMANCE

First, some physical quantities of the microscope will be mentioned. The effective magnification between the object and grating planes, given by the ratio of the focal lengths of the 50 mm camera objective and the microscope objective, see ***Section 4.1***, is $M_1 = f_{cam}/f_{obj} = 15.15$. Analogous the effective magnifications between the object plane and the CCD-camera and between the grating plane and the CCD-camera are $M_2 = 30.30$ and $M_3 = 2.0$, respectively. The normalized spatial frequency, described in ***Section 4.4.2***, is, for a grating with 23.5 lines·mm^{-1}, a wavelength of 514 nm (the central green wavelength is often used in microscopy due to the optical corrections of the objectives) and this particular microscope configuration, $\tilde{\nu} = 0.261$. The optimal spatial frequency, which is given for $\tilde{\nu} = 1$, is 92.4 lines·mm^{-1} and yields maximum sectioning.

In the rest of this section some tests and measurements, performed on the different components in the microscope, will be discussed.

6.1 Camera objectives

Initially it was intended to use camera optics from Goyo and the Pulnix CCD-camera. When it was not possible to image the original grating, see ***Section 6.2*** and ***Figure 16***, it was suggested that this was due to imaging aberrations. Thus, new optics, i.e. the Schneider-Kreuznach lenses, was purchased. Unfortunately, this did not help, the grating still could not be imaged, see ***Figure 16***.

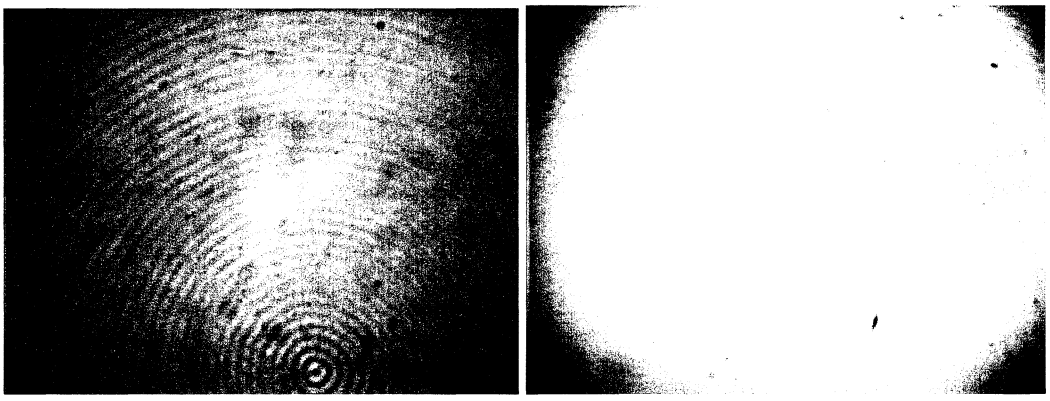

Figure 16: ***The 58.8 lines ·mm^{-1} grating could not be imaged when using either the Goyo camera lenses, left image, or the Schneider camera lenses, right image, combined with the Pulnix TM-860 CCD-camera. The circular pattern is superimposed on the grating.***

However, when Goyo optics was used unwanted glare degraded the images especially strong in the central portions of the images. Images acquired with the Schneider-Kreuznach optics did not suffer from such manifest glare. The difference is illustrated with images, acquired with the JAI-camera, in ***Figure 17***., which shows that the optical quality of the Schneider-Kreuznach objective lenses is better than that for the Goyo optics.

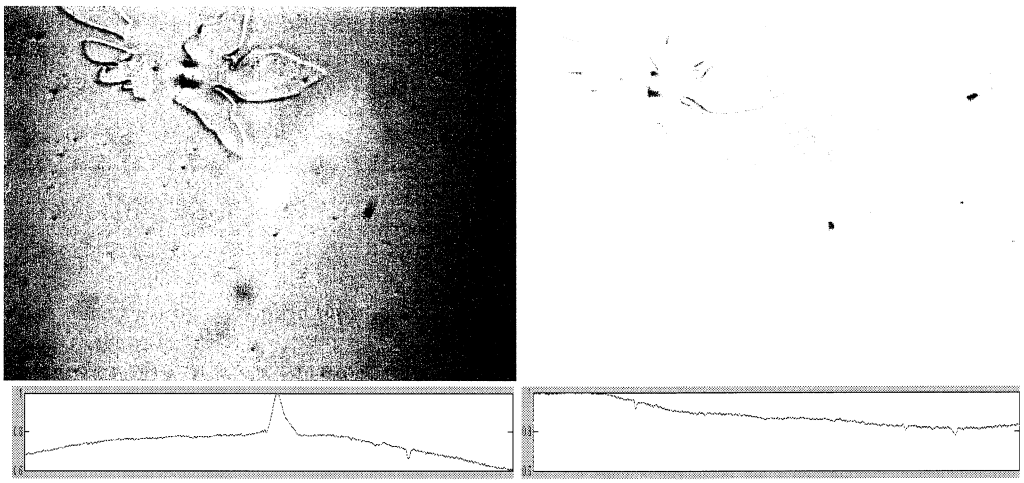

Figure 17: ***These images of a "white" surface were acquired with the JAI CV-M10 SX CCD-camera. The curves correspond to the sum of ten rows of pixels in the central part of each image. In both cases the light was attenuated with a 50 %-transmission grey-filter. For the acquisition of the left image, the Goyo camera lenses were used, and for the right image, the Schneider-Kreuznach lenses were used.***

6.2 Grating

When the project started, a transmission grating with a spatial frequency of 58.8 lines ·mm^{-1}, corresponding to a normalized spatial frequency of 0.654, was available. However, the attempts to image this grating did not succeed, as shown in ***Figure 16***. Since it was possible to image a test object, from a measuring microscope, placed at the grating plane, it was concluded that this was not due to misplacement of the grating. We guessed that the image quality in the Goyo lenses was not good enough, due to aberrations, to image the spatial frequency of the grating. Another hypothesis was that the entrance aperture at the back of the objective lens cut off parts of the modulated light. The diffraction orders of a grating with lower spatial frequency will be less spread. Thus, more light will be gathered by the objective lens.

It was decided that a new grating, with a spatial frequency of 23.5 lines·mm^{-1}, should be manufactured. This particular spatial frequency was chosen because we were able to image the original grating with the 50 mm lens replaced by a 20 mm achromat. Thus, the effective magnification, with the achromat used, differs by a factor of 2.5. To get the same spatial frequency of the projection of the grating at the object plane when using the 50 mm camera lens as when the 20 mm achromat is used, the new grating, thus, should have 58.8/2.5 = 23.5 lines·mm^{-1}. Note that when the microscope is operated with the new grating, a total elongation of the actuator of 28.3 μm is needed; corresponding to a translation of the grating by the same distance. This is very close to the actuator's physical limit.

The grating was made in a holographic setup. The cosine-pattern was produced by having two expanded laser beams interfere at a photographic plate. The plate should not be bleached during the development. A Michaelson interferometer setup was used to expose a photographic plate. By tilting one of the mirrors sideways the interference pattern could be controlled according to $\nu \cdot \sin\theta = \lambda/2$, where ν is the spatial frequency, λ the laser wavelength and θ the angle the mirror is tilted.

Some exposures, with different plates and exposure times, and developments were carried out before we were satisfied with the result. The gratings produced were evaluated by power measurements of the diffraction orders. In ***Table 1*** the measurement results are presented. From Fourier optics it is known that a perfect cosine-grating has

only the 0th and the ±1st diffraction orders.[51] Based on this, the gratings from exposures 3 and 4 were excluded, since they both suffered from comparably strong 2nd and 3d order light. Also, it has been shown the maximum ratio of the power in the first order to the power of the incident light is 0.0625.[51] Therefore, the gratings from exposures 1 and 2 were both good candidates. However, since the grating from exposure 2 has a larger ratio between light in its 1st orders compared to the 0th order, indicating a better modulation depth, this grating was used in the microscope.

Table 1: ***Measurements of light power in the various diffraction orders of gratings from four exposures of a photographic plate. The ratios of the power in the diffraction orders to the power of the incident light and to the power in the 0th order are also presented.***

Exposure:	Power (μW):			Power ratio to incident light:		Power ratio to 0th order:	
	0	+1	-1	+1	-1	+1	-1
1	12.58	2.28	2.238	0.041	0.040	0.181	0.178
2	6.38	2.071	2.065	0.037	0.037	0.325	0.324
3	4.17	1.819	1.845	0.032	0.033	0.436	0.442
4	1.311	0.803	0.791	0.014	0.014	0.613	0.603
Incident light intensity:			56.1 μW				

When the new JAI-camera was used, later in the project, the hypothesis about the entrance of the objective lens cutting off some of the important parts of the light proved not to be completely true. It was possible to image the old grating with this camera. However, the modulation of the new grating was much better then that of the old one, see ***Figure 18***. Also, a circular pattern, superimposed on the grating, is visible on the old grating. This is probably due to diffraction in the setup used to produce the grating.

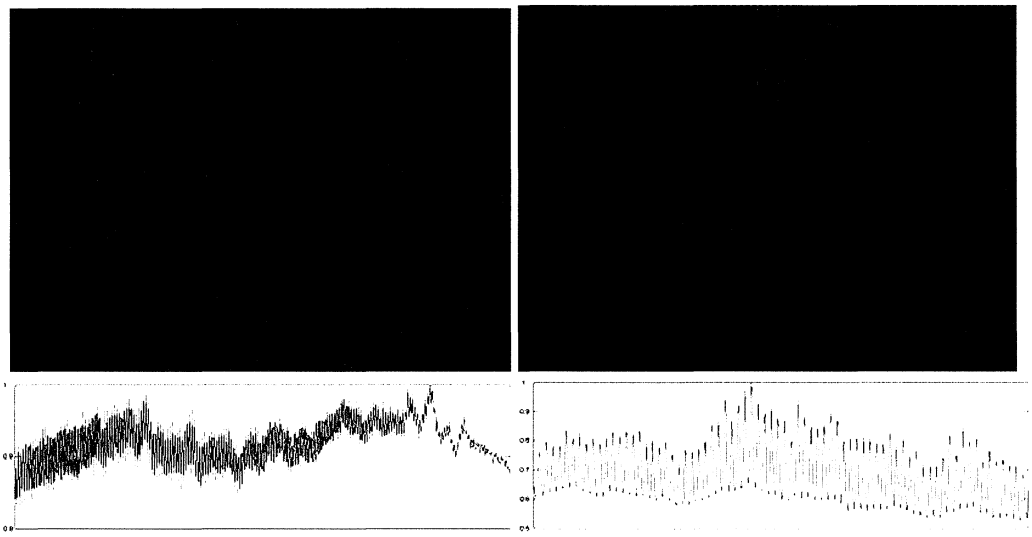

Figure 18: ***The difference in modulation between the 58.8 lines ·mm^{-1} and 23.5 lines·mm^{-1} gratings can be illustrated with these two images, acquired with the JAI CV-M10 SX CCD-camera. The left image is from the 58.8 lines ·mm^{-1} grating and the right from the 23.5 lines·mm^{-1} grating. Notice the circular pattern superimposed on the 58.8 lines ·mm^{-1} grating. The curves below the images illustrate the difference in modulation, which can be estimated to 0.1 and 0.3 for the 58.8 lines·mm^{-1} and 23.5 lines·mm^{-1} gratings, respectively.***

6.3 Piezoelectric actuator and control unit

In order to be able to get a well-defined displacement of the grating, the piezoelectric actuator had to be calibrated. Once again the principle of a Michaelson interferometer was used, with one of the mirrors mounted on the actuator, perpendicular to its displacement axis. If the difference between the two arm-lengths of the interferometer is equal to a multiple a half wavelength of the illumination light, the centre of the resulting Bessel patterns at the detection screen appears to be dark. The voltage applied to the actuator by the control unit was slowly increased from 0 V to 100 V. The voltage was recorded for each new dark centre appearing on the screen. In ***Figure 19*** the resulting calibration curve, were the elongation of the actuator has been plotted to the voltage of the power box, is displayed. In total, the voltage corresponding to 98 dark centres was recorded and, as can be seen in the figure, the dependence is quite linear.

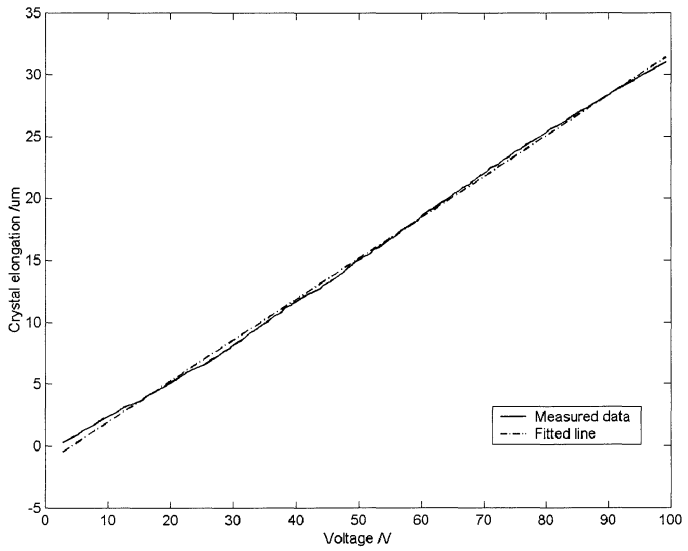

Figure 19: ***Calibration curve for the piezoelectric actuator. The solid curve corresponds to the measures data and the dashed line is the strait line approximation fitted to the data.***

7 SAMPLE MEASUREMENTS

During the development of the microscope, several test objects have been used. To investigate the performance of the optics and the imaging of the grating a white painted object glass was used. It was turned with is back towards the microscope objective to get an optically flat surface. This white flat object can also be used to confirm that adding the three images, with relatively displaced grid patterns, result in the conventional microscope image. This is shown in ***Figure 20***, which also illustrates the importance of correct grid translation. The grid pattern will not be completely removed if the grating is not translated to the correct positions.

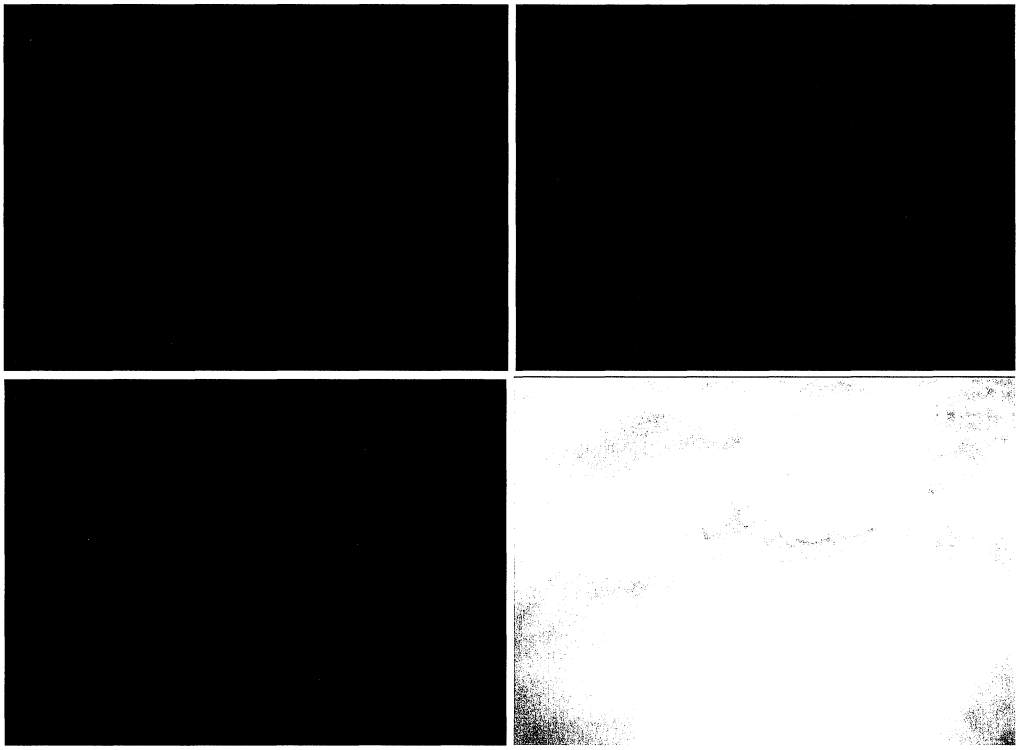

Figure 20: ***Equation X.X can be confirmed by adding the three images of the grating, in this case acquired with the JAI CV-M10 SX CCD-camera. The result, shown in the bottom right image, is the conventional microscope image. It is important that the grating is translated the exact 1/3 of the spatial frequency. Otherwise the grid pattern will not be removed completely.***

A couple of test objects with hair, embedded in epoxy, were made. An object glass and a cover glass were squeezed together with the hair and epoxy mixture between them. To get a well-defined thickness of the object, another object glass where cut in pieces, which were placed surface-to-surface with the object glass and the cover glass. Unfortunately, the epoxy turned highly scattering and slightly grey when hardening. Thus, the absorption and scattering ruined the images acquired of this object. It was hard even to image the hair at the surface of the object.

To prevent the epoxy from blurring the image, an object with a single hair, attached in the ends to an object glass, was made. This object was used during test with all three CCD-cameras. With the Pulnix-camera the resulting image was highly dominated by noise and, in fact, nothing else could really be seen in the attempts of optical sectioning using ***Equation 20***, see ***Figure 21***.

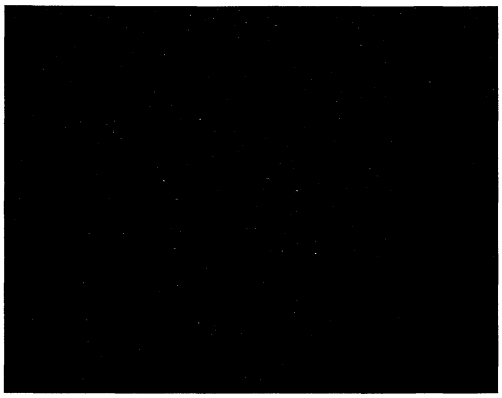

Figure 21: ***When the Pulnix TM-860 CCD-camera was used for the sectioning algorithm, the information completely blurred due to the too noisy image acquisition.***

The result, when the camera from Princeton Instruments, Inc. was used, was better. The camera was set to have a shutter time of 100 ms and ten images were acquired and added in the computer. ***Figure 22*** shows three raw images as well as the optically sectioned image produced with this scientific grade CCD-camera in the setup. The grating is focused only in a single plane of the three-dimensional object. This is the reason why the raw images do not display a visible grid pattern.

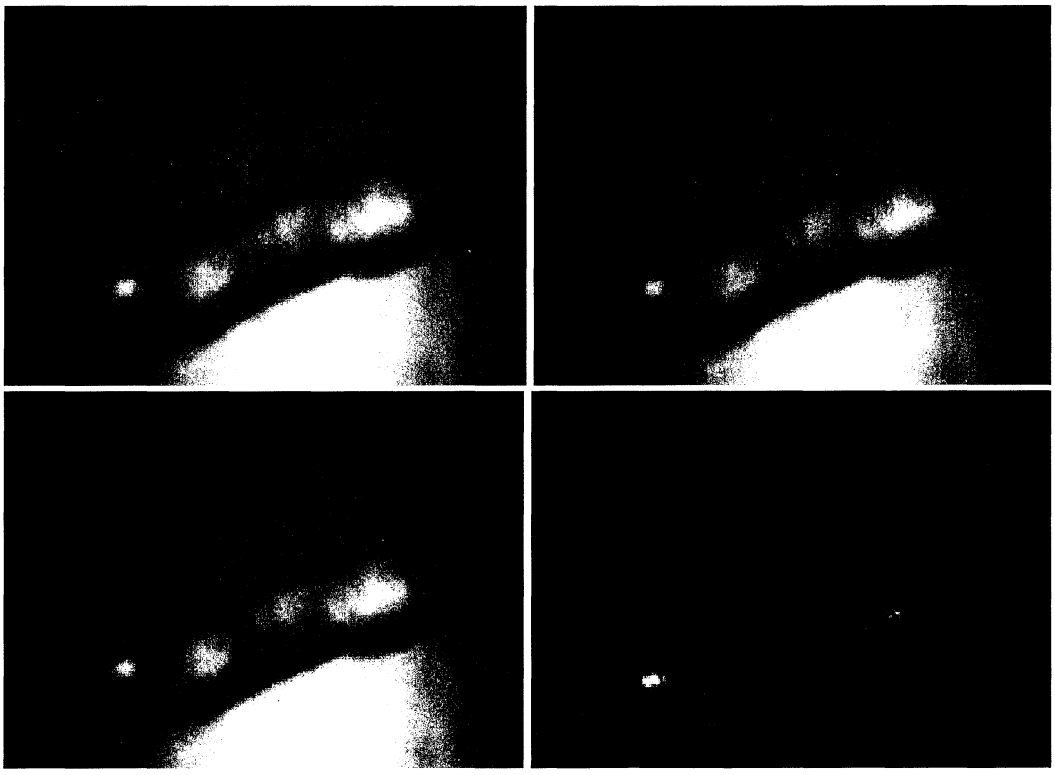

Figure 22: ***The upper images and the lower left image are acquired with a translation of the grating, corresponding to 1/3 of the grating period, between each acquisition. The lower right image is the optical sectioned image, calculated from the other three, of a hair on an object glass. The camera used was the Princeton Instruments, Inc. camera.***

Finally, the JAI-camera was used. A LabVIEW-script was written to acquire and add ten images, just as for the cooled-CCD. The result is displayed to the right in ***Figure 23***. The left image of ***Figure 23*** shows the resulting sectioned image when the LabVIEW-script is not used and only one readout is done per image. The impact of camera noise on the image quality will de discussed in the next chapter.

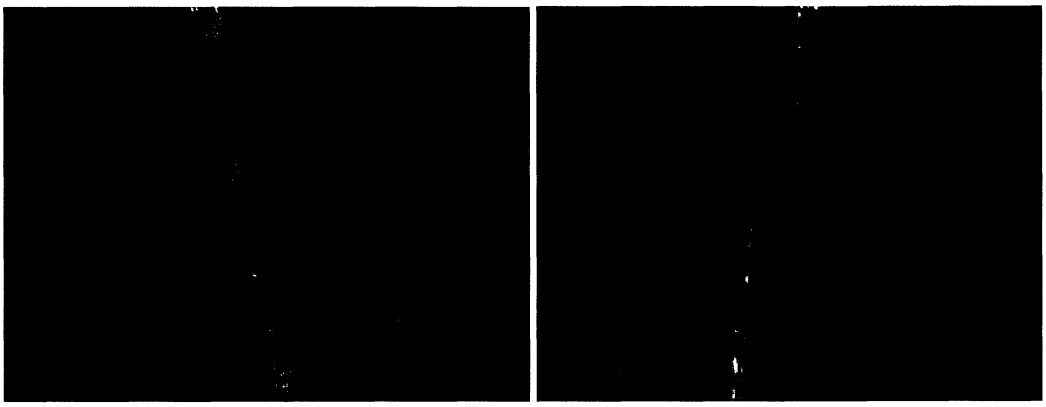

Figure 23: ***The images are the result of applying the optical sectioning algorithm to images of a hair, acquired with the JAI CV-M10 SX CCD-camera. During acquisition of the raw images for the left image, one single readout of the CCD was made per image. For the right image, ten readouts were made and added for each raw image.***

8 DISCUSSION

From studying the images in the preceding chapter, we have found that high dynamic range in the detection, by which we mean high signal and low noise levels, is vital to the result of optical sectioning. High dynamics also allows better usage of the resolution in the optical system, as the image becomes less noisy. Noise in the detection system plays an important role to the dynamics. Photon noise, which is a physical limitation of noise due to the statistical variation in photon density of the light incident to the CCD-chip, was discussed in ***Section 4.1.3***. The photon noise is according to statistical theory, under all circumstances, proportional to the square root of the average number of photons in the signal and, thus, we cannot do anything to reduce it. The effect of the photon noise is, however, affected by the characteristics of the detector. *Dark current* is a signal generated in the camera due to thermal relaxation. This signal can be subtracted from the real signal, but the noise related to it is non-subtractable. This noise will, thus, degrade the image slightly. In images acquired with a camera that suffer from a high level of dark current, the maximum intensity of the real signal will also decrease before the camera saturates. Thus, it will also reduce the signal-to-noise ratio in this sense. Another type of camera noise is *readout noise*. Readout noise is added to the signal when the pixels on the CCD-chip are read.

In confocal microscopy most of the light from the object is blocked by the pinhole before detecting the signal from the point in focus. In the optical sectioning microscope built in this project all the light from the object is detected first. Then, when the sectioning algorithm, ***Equation 20***, is applied most of the signal is filtered out, and only the signal from the focal plane is extracted. Unfortunately, this does not apply for the noise. This will result in a drastic decrease in signal-to-noise ratio in the image formed by subtraction of two images with comparable intensity, as illustrated by ***Figure 24***. This implies that a low level of noise is important to the method used. The influence of dark current noise and readout noise can be reduced by cooling the CCD-chip and decrease the rate of information transfer from the chip, respectively. This is the reason why the best result was achieved with the Princeton Instruments, Inc. CCD-camera. As was mentioned in ***Section 5.3*** this camera was cooled to -60 °C with liquid-nitrogen and had a rather long readout time.

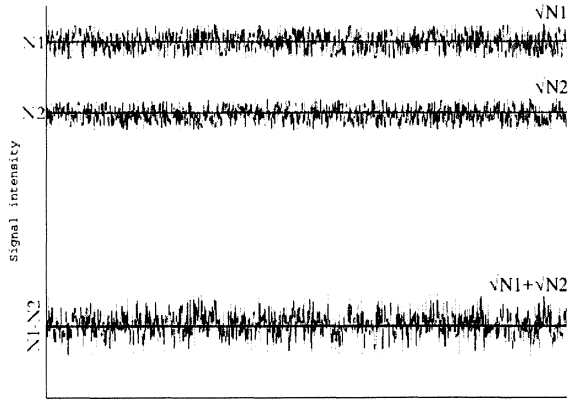

Figure 24: ***Two signals with the comparable intensities N1 and N2 experience noise with a magnitude of √N1 and √N2, respectively. If the signals are subtracted, the level of the resulting signal will be close to zero while the noise will be equal to √N1 + √N2. Thus, the signal-to-noise ratio is decreased drastically.***

During the transmission of the analogue signal from the camera to the framegrabber, further noise is added to the image as mentioned above. If I had known from the beginning that I had to replace the Pulnix camera, I would probably choose a fire wire camera instead of both camera and framegrabber. Images from such a camera do not suffer from the same amount of noise due to the image transfer, since digital signals are less sensitive to noise than analogue ones. Also, there would be roughly twice the money to spend on a high quality camera if I had not bought a framegrabber as well.

In the future, when the microscope is further developed to be used to study red blood cells flowing in a cuvette, some aspects of the instrument should be reviewed. First of all, the piezoelectric actuator has to be calibrated by measuring the translation due to the application of a large voltage step. Its behaviour is probably not as linear in this case.

The actuator control unit available suffer from extreme voltage fluctuation; the voltage can vary up to 10 %. Therefore, it is recommended that the control unit is replaced by the commercial Physik Instrumente control unit available. This would produce a stable voltage and more exact control of the actuator.

The grating is another part I would like to replace. The surface of the existing grating is rather patchy. If is desirable that the grating has a level and clean surface, since it is located in a plane conjugate to the object plane, not to deteriorate the illumination. I would recommend buying a commercial cosine-grating, which can also have better modulation. Using a Ronchi-grating could also be considered, since this has proved to work as well and is more light-efficient.[5] The exact positioning of such grating would, however, be much more critical due to the sharp edges.

A limiting factor of the performance during measurement of moving objects is the time the actuator requires translating the grating. Other ways to translate the grating should, thus, be considered.

9 CONCLUSION

In conclusion, we have built a compact microscope system for optical sectioning. The optical sectioning is achieved by introducing a single spatial frequency in the illumination followed by extraction of this frequency from the images. Thus, the primary objective of this project is achieved. The properties of images acquired with such system are comparable to the properties of images from an optical scanning confocal microscope. The result is, however, strongly depending of the signal-to-noise ration in the detected signal. Some suggestions for improved operation have been given.

We did not fully reach the secondary objective, to study red blood cells in whole-blood flowing through a thin cuvette. This is, however, the next step in the development process and a cuvette is already designed and constructed. It is our intention to test this within a near future.

10 ACKNOWLEDGEMENTS

First of all, I would like to thank my supervisors Stefan Andersson-Engels and Johannes Swartling for his assistance during the project and patience with my questions. I would also take the opportunity to thank Nels Hansson at the Workshop at the Department of Astronomy who has assisted during design of the specialized parts in the system and also manufactured them. Finally, I would like to thank Sven-Göran Pettersson who has been of great help during the construction of the new gratings.

This project was financially supported by the Craaford foundation.

11 REFERENCES

1 M. A. A. Neil, R. Juskaitis, T. Wilson, "Method of obtaining sectioning by using structured light in a conventional microscope", *Opt. Lett.* **22**, pp. 1905-1907 (1997)

2 M. J. Cole, J. Siegel, S. E. D. Webb, R. Jones, K. Dowling, P. M. W. French, M. J. Lever, L. O. D. Sucharov, M. A. A. Neil, R. Juškaitis, T. Wilson, "Whole-field optically sectioned fluorescence lifetime imaging", *Opt. Lett.* **25**, pp. 1361-1363 (2000).

3 M. J. Cole, J. Siegel, S. E. D. Webb, R. Jones, K. Dowling, M. J. Dayel, D. Parsons-Karavassilis, P. M. W. French, M. J. Lever, L. O. D. Sucharov, M. A. A. Neil, R. Juškaitis, T. Wilson, "Time-domain whole-field fluorescence lifetime imaging with optical sectioning", *J. Microsc.* **203**, pp. 246-257 (2000).

4 J. Siegel, D. S. Elson, S. E. D. Webb, D. Parsons-Karavassilis, S. Lévêque-Fort, M. J. Cole, M. J. Lever, P. M. W. French, M. A. A. Neil, R. Juškaitis L. O. Sucharov, T. Wilson, "Whole-field five-dimensional fluorescence microscopy combining lifetime and spectral resolution with optical sectioning", *Opt. Lett.* **26**, pp. 1338-1340 (2001).

5 D. S. Elson, J. Siegel, S. E. D. Webb, S. Lévêque-Fort, D. Parsons-Karavassilis, M. J. Cole, P. M. W. French, D. M. Davis, M. J. Lever, R. Juškaitis, M. A. A. Neil L. O. Sucharov, T. Wilson, "Wide-field fluorescence lifetime imaging with optical sectioning and spectral resolution applied to biological samples", *J. Mod. Optic.* **49**, pp. 985-995 (2002).

6 S. E. D. Webb, S. Lévêque-Fort, D. S. Elson, J. Siegel, T. Watson, M. J. Lever, M. Booth, R. Juškaitis, M. A. A. Neil L. O. Sucharov, T. Wilson, P. M. W. French, "Wavelength-Resolved 3-Dimensional Fluorescence Lifetime Imaging", *J. Fluoresc.* **12**, pp. 279-283 (2002).

7 E. Hecht, *Optics*, 2nd ed., Addison-Wesley Publishing Company, Inc., USA (1987).

8 F. L. Pedrotti, L. S. Pedrotti, *Introduction to optics*, 2nd ed., Prentice-Hall, Inc., New Jersey, USA (1993).

9 A. J. Welch, M. J. C. van Gemert, *Optical-thermal response of laser-irradiated tissue*, Plenum Press, New York, USA (1995).

10 C. af Klinteberg, *On the use of light for the characterization and treatment of malignant tumours*, PhD Thesis, Department of Physics, Lund Institute of Technology, Lund, Sweden (1999).

11 G. M. Hale, M. R. Querry, "Optical constants of water in the 200-nm to 200-μm wavelength region", *Appl. Opt.* **12**, pp. 555-563 (1973).

12 S. A. Prahl, "Tabulated molar extinction coefficient for hemoglobin in water", accessed 30 January 03 2003 11:55, (1998). http://omlc.ogi.edu/spectra/hemoglobin/summary.html

13 C. Eker, *Optical characterization of tissue for medical diagnostics*, PhD Thesis, Department of Physics, Lund Institute of Technology, Lund, Sweden (1999).

14 G. J. Tortora, S. R. Grabowski, *Principles of anatomy and physiology*, 8th ed., HarperCollins Publishers Inc., New York, USA (1996).

15 S. L. Jacques, D. J.McAuliffe, "The melanosome: Threshold temperature for explosive vaporization and internal absorption coefficient during pulsed laser irradiation", *Photochem. Photobiol.* **53**, pp.769-775, (1991). Also found at http://omlc.ogi.edu/spectra/melanin/mua.html

16 S. Svanberg, *Atomic and Molecular Spectroscopy - Basic Aspects and Practical Applications*, 3d ed., Springer-Verlag, Berlin Heidelberg, Germany (2001).

17 L. G. Henyey, J. L. Greenstein, "Diffuse radiation in the galaxy", *Astrophys. J.* **93**, pp. 70-83. (1941).

18 G. J. Tearney, M. E. Brezinski, J. F. Southern, B. E. Bouma, M. R. Hee, J. G. Fujimoto, "Determination of the refractive index of highly scattering human tissue by optical coherence tomography", *Opt. Lett.* **20**, pp. 2258-2260 (1995).

19 F. P. Bolin, L. E. Preuss, R. C. Taylor, R. J. Ference, "Refractive index of some mammalian tissues using a fiber optic cladding method", *Appl. Opt.* **28**, pp. 2297-2303 (1989).

20 A. M. K. Enejder, *Light scattering and absorption in tissue – models and measurements*, PhD Thesis, Department of Physics, Lund Institute of Technology, Lund, Sweden (1997).

21 J. Beuthan, O. Minet, J. Helfmann, M. Herrig, G. Müller, "The spatial variation of the refractive index in biological cells", *Phys. Med. Biol.* **41**, pp. 369-382 (1996).

22 J. R. Mourant, J. P. Freyer, A. H. Heilscher, A. A. Eick, D. Shen, T. M. Johnson, "Mechanisms of light scattering from biological cells relevant to noninvasive optical-tissue diagnostics", *Appl. Opt.* **37**, pp. 3586-3593 (1998).

23 J. Sørensen Dam, *Optical analysis of biological media – continuous wave diffuse spectroscopy*, PhD Thesis, Department of Physics, Lund Institute of Technology, Lund, Sweden (2000).

24 S. A. Prahl, M. Keijzer, S. L. Jacques, A. J. Welch, "A Monte Carlo Model of Light Propagation in Tissue", *SPIE Institute Series Vol. IS 5 - Dosimetry of Laser Radiation in Medicine and Biology* (1989).

25 A. C. Guyton, *Function of the human body*, 3d ed., W.B. Saunders Company, Philadelphia, USA (1969).

26 A. M. K Enejder, J. Swartling, P. Aruna, S. Andersson-Engels, "Influence of cell shape and aggregate formation on the optical properties of flowing whole blood", *Appl. Opt.* **42**, pp. 1384-1394 (2003).

27 J. M. Steinke, A. P. Shepherd, "Comparison of Mie theory and the light scattering of red blood cells", *Appl. Opt.* **27**, pp. 4027-4033 (1988).

28 A. M. K. Nilsson, C. Sturesson, D. L. Liu, S. Andersson-Engels, "Changes in spectral shape of tissue optical properties in conjuction with laser-induced thermotherapy", *Appl. Opt.* **37**, pp. 1256-1267 (1998).

29 M. Hammer, A. N. Yaroslavsky, D. Schweitzer, "A scattering phase function for blood with physiological haematocrit", *Phys. Med. Biol.* **46**, pp. N65-N69 (2001).

30 A. N. Yaroslavsky, I. V. Yaroslavsky, T. Goldbach, H.-J. Schwarzmaier, "Influence of the scattering phase function approximation on the optical properties of blood determined from the integrating sphere measurements", *J. Biomed. Opt.* **4**, pp. 47-53 (1999).

31 A. Roggan, M. Friebel, K. Dörschel, A. Hahn, G. Müller, "Optical properties of circulating human blood in the wavelength range 400-2500 nm", *J. Biomed. Opt.* **4**, pp. 36-46 (1999).

32 A. M. K. Nilsson, G. W. Lucassen, W. Verkruysse, S. Andersson-Engels, M. J. C. van Gemert, "Changes in optical properties of human whole blood *in vitro* due to slow heating", *Photochem. Photobiol.* **65**, pp. 366-373 (1997).

33 A. M. K. Nilsson, P. Alsholm, A. Karlsson, S. Andersson-Engels, "T-matrix computations of light scattering by red blood cells", *Appl. Opt.* **37**, pp. 2735-2748 (1998).

34 Molecular Expressions Microscopy Primer, accessed 24 November 2003 12:00. http://micro.magnet.fsu.edu/primer/museum/janssen.html

35 Molecular Expressions Microscopy Primer, accessed 22 October 2003 16:06. http://micro.magnet.fsu.edu/primer/anatomy/tubelength.html

36 M.W. Davidson, M. Abramowitz, "Optical Microscopy", at the Molecular Expressions Microscopy Primer, accessed 15 August 2003 12:00. http://micro.magnet.fsu.edu/primer/opticalmicroscopy.html

37 R. C. Gonzalez, R. E Woods, *Digital Image Processing*, 2nd ed., Prentice-Hall Inc., New Jersey, USA (2002).

38 Molecular Expressions Microscopy Primer, accessed 10 November 2003 10:45. http://micro.magnet.fsu.edu/primer/anatomy/numaperture.html

39 R. H. Webb, "Confocal optical microscopy", *Rep. Prog. Phys.* **59,** pp. 427-471 (1996).

40 Nikon MicroscopyU, accessed 10 November 2003 10:45. http://www.microscopyu.com/articles/formulas/formulasfielddepth.html

41 M. Pluta, *Advanced Light Microscopy vol. 1 Principles and Basic Properties*, Elsevier Science Publishers, Amsterdam, The Netherlands (1988).

42 M. Pluta, *Advanced Light Microscopy vol. 2 Specialized Methods*, Elsevier Science Publishers, Amsterdam, The Netherlands (1989).

43 Molecular Expressions Microscopy Primer, accessed 22 October 2003 16:05. http://micro.magnet.fsu.edu/primer/anatomy/objectives.html

44 Molecular Expressions Microscopy Primer, accessed 23 December 2003 12:10. http://micro.magnet.fsu.edu/primer/java/microscopy/immersion/index.html,

45 Molecular Expressions Microscopy Primer, english translation of: A. Köhler's *A New System of Illumination for Photomicrographic Purposes*, accessed 20 September 2003 10:00. http://micro.magnet.fsu.edu/primer/anatomy/kohleroriginal.html

46 J. B. Pawley, *Handbook of Biological Confocal Microscopy*, Plenum Press, New York, USA (1990).

47 T. Wilson, *Confocal Microscopy*, Academic Press Limited, London, UK (1990).

48 T. Wilson, M. A. A. Neil, R. Juškaitis, "Real-time three-dimensional imaging of macroscopic structures", *J. Microsc.* **191**, pp. 116-118 (1998).

49 Z. Ansari, Y. Gu, J. Siegel, R. Jones, P. M. W. French, D. D. Nolte, M. R. Melloch, "Wide-field, real-time depth-resolved imaging using structured illumination with photorefractive holography", *Appl. Phys. Lett.* **81**, pp. 2148-2150 (2002).

50 C.-H. Lee, H.-Y. Mong, W.-C. Lin, "Noninterferometric wide-field optical profilometry with nanometer depth resolution", *Opt. Lett.* **27**, pp. 1773-1775 (2002).

51 S.-G. Pettersson, S. Borgström, H. Hertz, *Advanced Optics*, Department of Physics, Lund Institute of Technology, KFS, Lund, Sweden (1999).

APPENDIX A - SMA FIBRE COUPLING

The fibre, which leads the light into the system, is mounted in an SMA-connector adjusting device. ***Figures 25*** through ***29*** shows the drawings for the components that comprise this device. The mounting ring slides in the mounting block when the adjusting plug is screwed in its mounting plate. The mounting ring is held in place by a feather pushing on the back of the ring. The feather is counter supported by the feather stop, which is placed in a standard *Holder 30*. All the parts for this device are manufactured of aluminium.

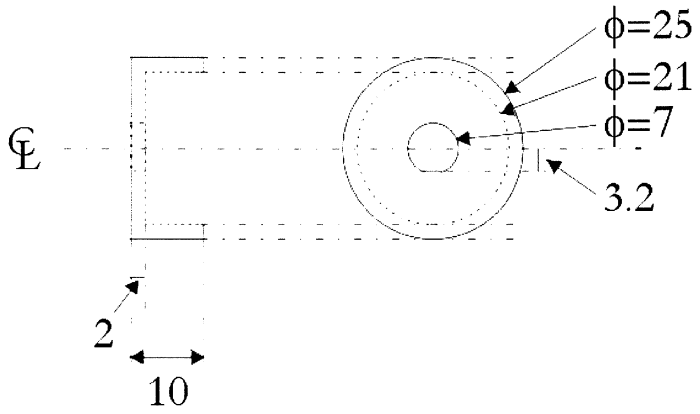

Figure 25: ***Mounting ring for SMA fibre coupling. An SMA-fibre connector is placed in the central hole.***

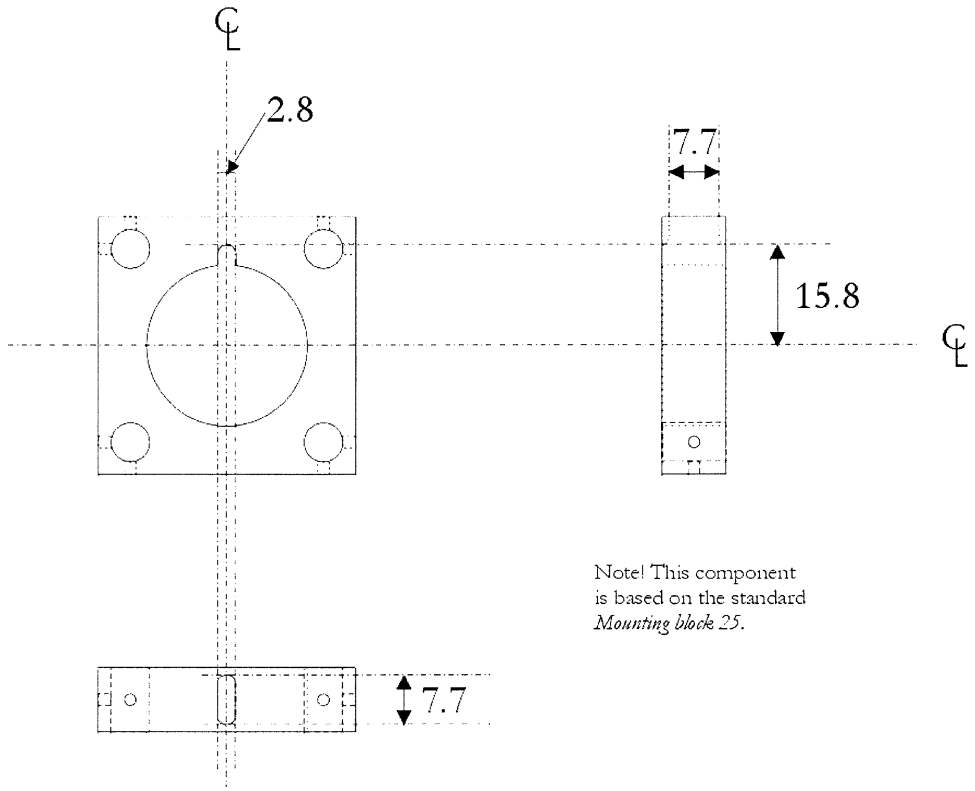

Figure 26: ***Mounting block 25 for SMA fibre coupling. The***

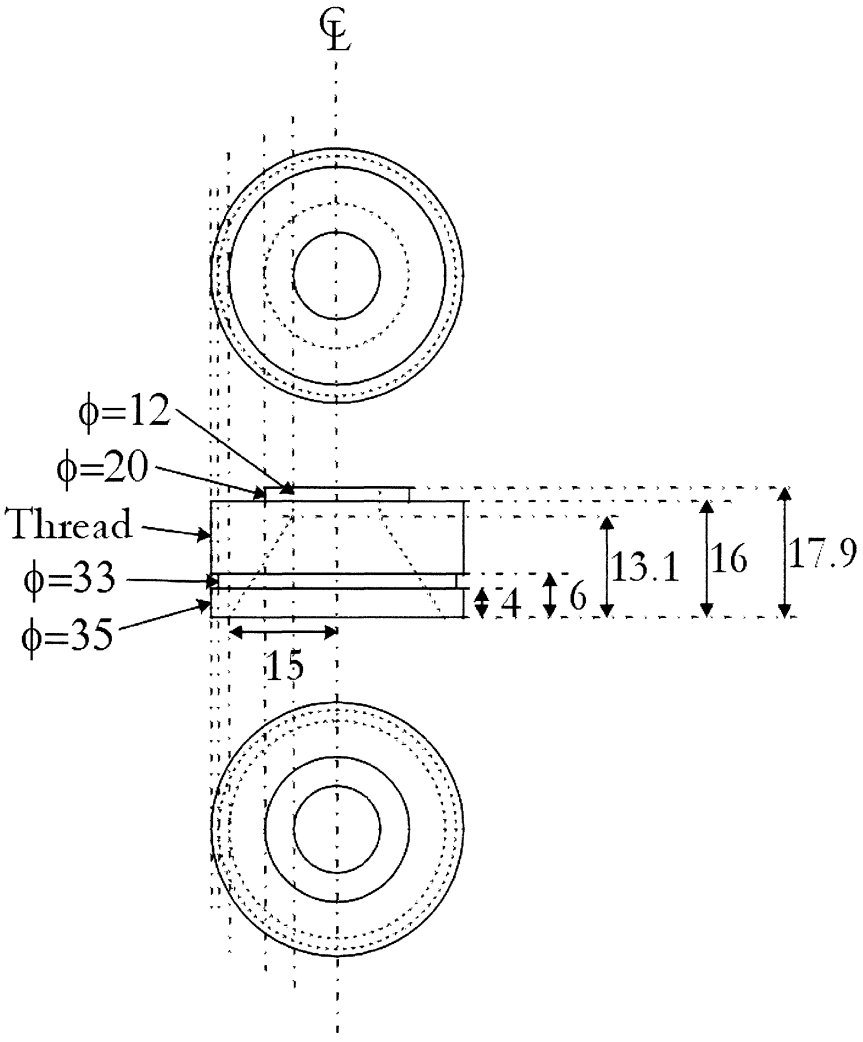

Figure 27: Adjusting plug for SMA fibre coupling.

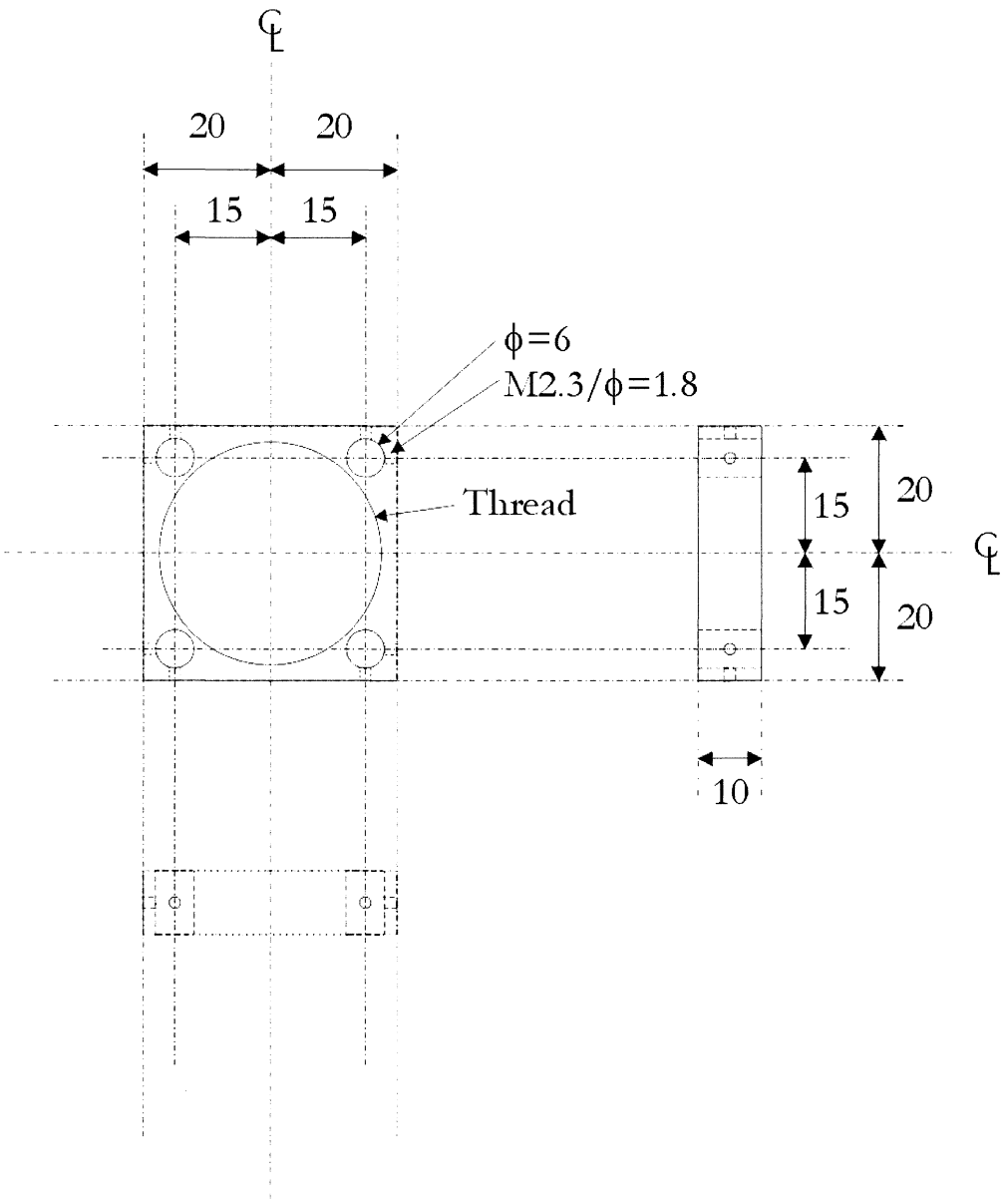

Figure 28: Mounting plate for the adjustment plug for SMA fibre coupling.

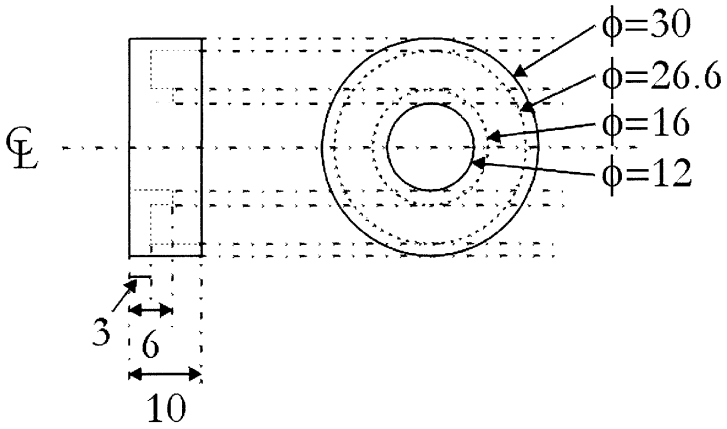

Figure 29: Feather stop for SMA fibre coupling.

APPENDIX B - ACTUATOR MOUNT

The piezoelectric actuator is mounted horizontally in the system with a component described by the drawing in ***Figure 30***. This mount component is made out of aluminium.

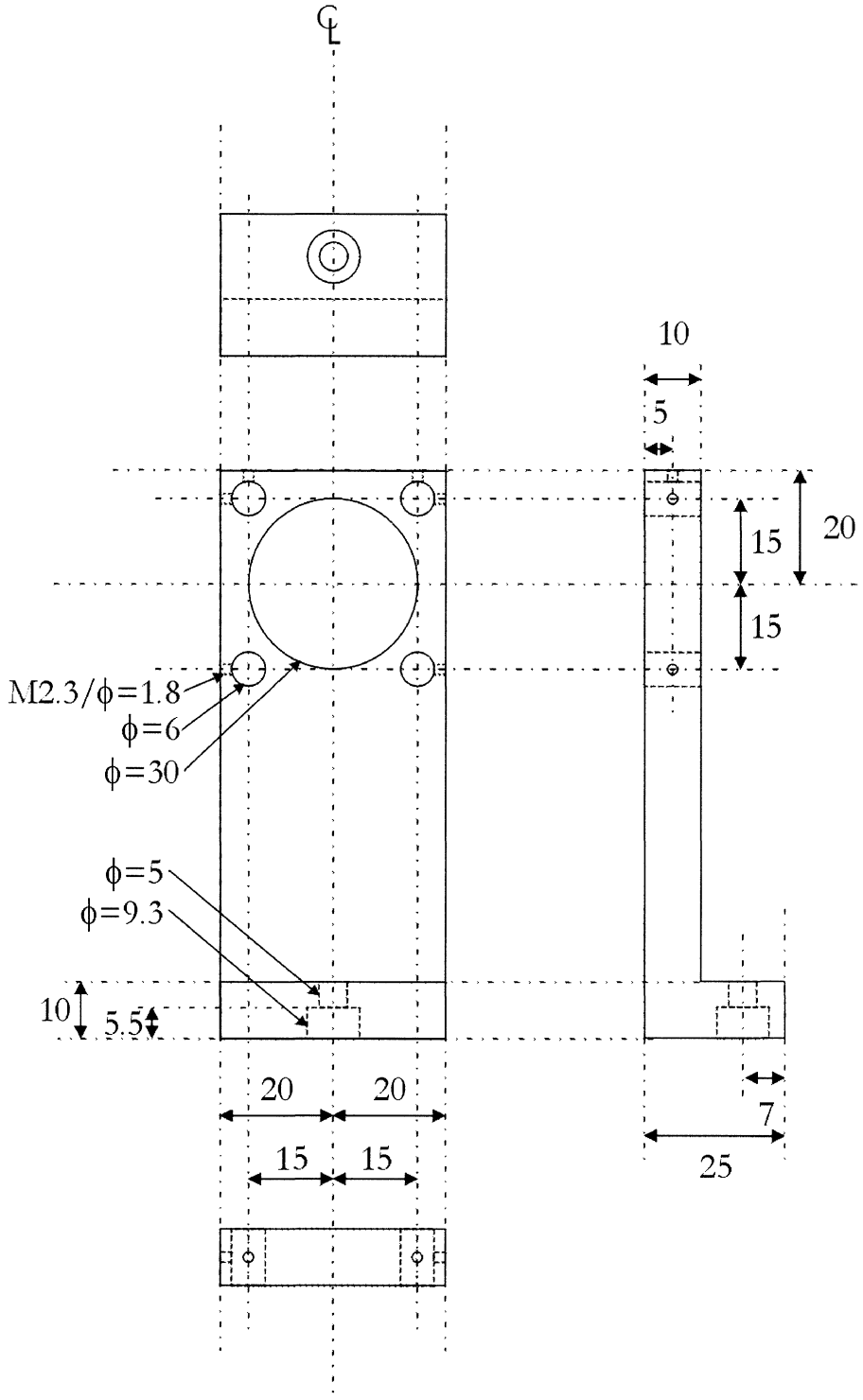

Figure 30: ***Mounting block for the piezoelectric actuator.***

APPENDIX C - BEAM-DEFLECTOR MOUNT

The Beam-deflector cube 30 is mounted on a block designed as ***Figure 31*** illustrates to stabilize the setup. The mounting block is made of aluminium.

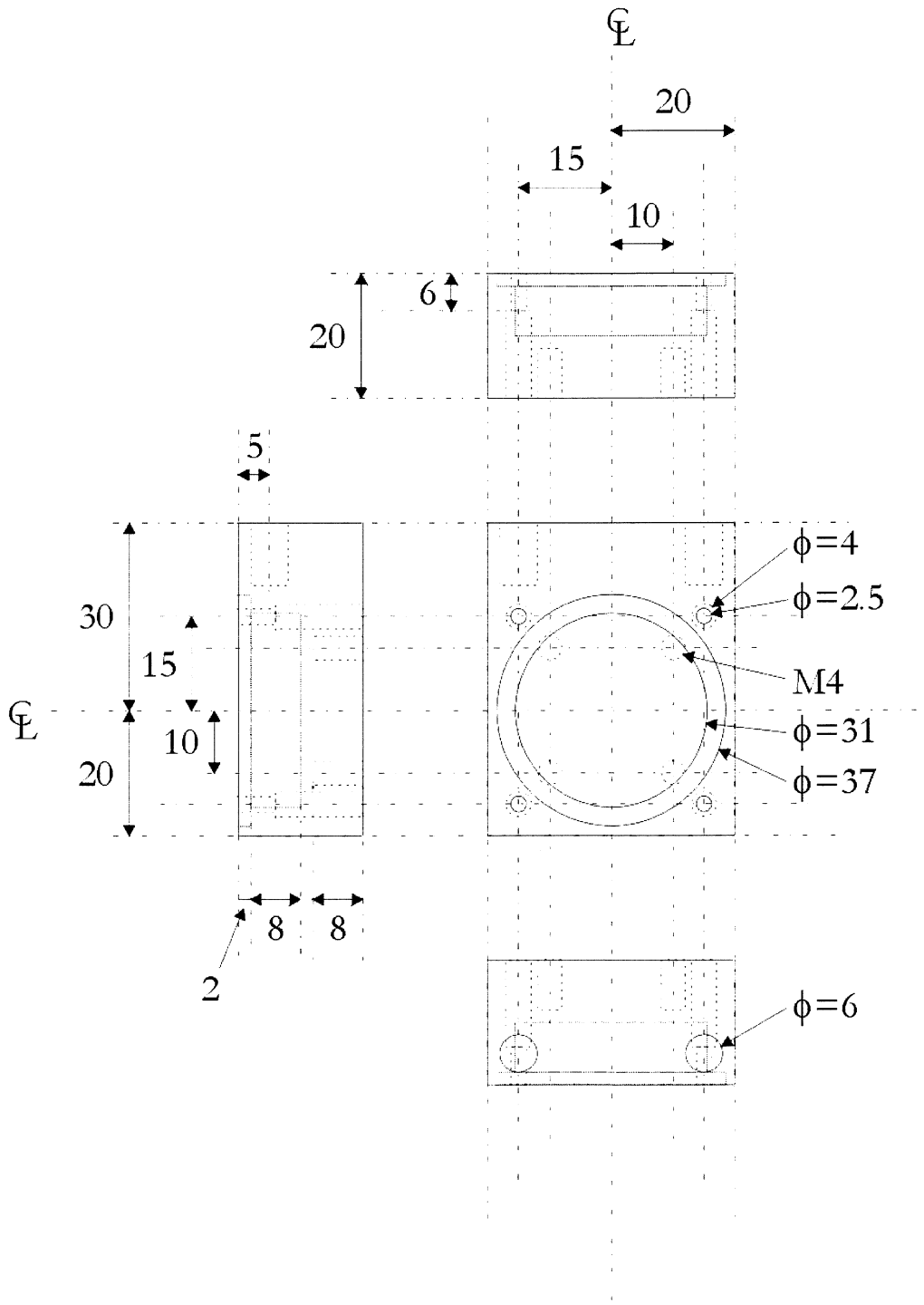

Figure 31: Mounting block for the beam-deflector cube.

APPENDIX D - BEAMDUMP

The beamdump, which collects the light lost in the first reflection at the beamsplitter, is made out of three separate components described in ***Figures 32*** through ***34***. With the holder the beamdump is attached to the bottom plate of the setup. The beambump cylinder is screwed tightly into the holder and then the cone is screwed to the cylinder. Light entering the beamdump is scattered at the smooth, gloss black surface of the cone to the rough inner wall of the cylinder. The beambump components are made of aluminium.

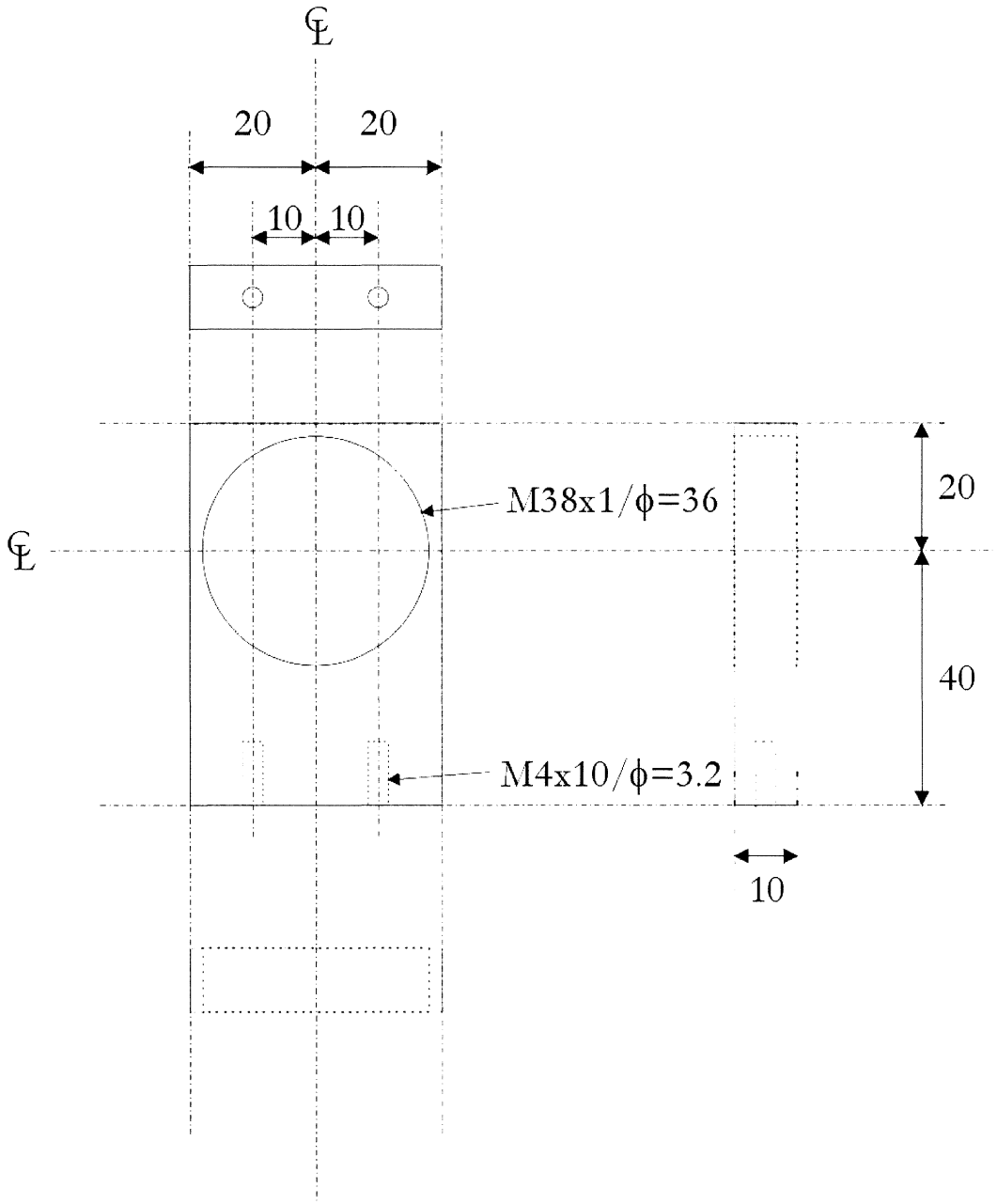

Figure 32: The holder for the beamdump is used to attach the beamdump to the bottom plate.

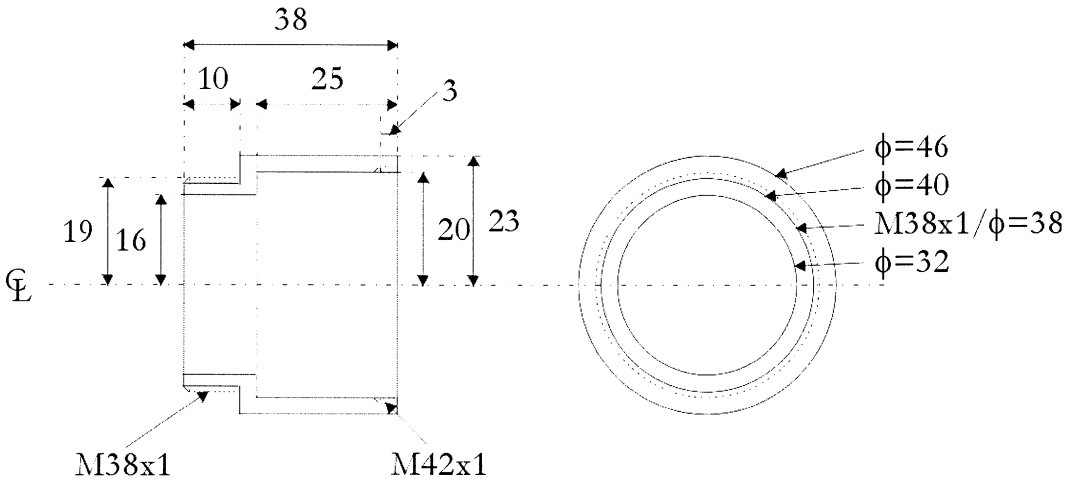

Figure 33: ***The beamdump cylinder has a rough black inner surface to which the light is scattered from the cylinder.***

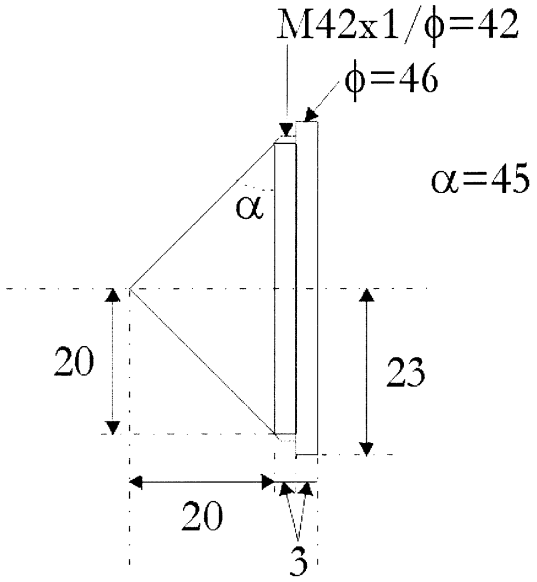

Figure 34: ***The surface of the beamdump cone smooth and gloss black. The incident light is absorbed and scattered to the cone.***

APPENDIX E - LENS MOUNT

Camera lens 2, which focuses the light from the objective lens to the CCD-chip, is mounted directly to the beam-deflector cube. This is done by a mounting ring constructed according to the drawing in ***Figure 35***. The ring is made of aluminium and the thread is made to fit the filter thread of the camera lens.

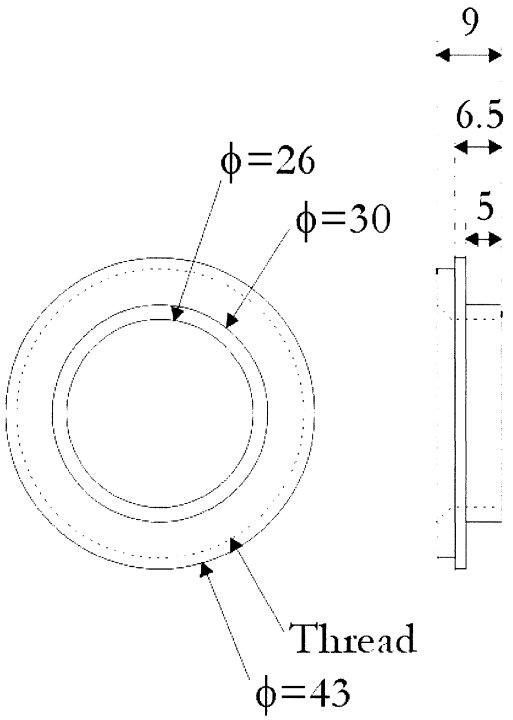

Figure 35: ***The mounting ring for the camera lens has a thread that fits the filter thread of the camera lens.***

APPENDIX F - CUVETTE

The metal parts of the cuvette are made of stainless steel. Aluminium cannot be used since the intention is to use the cuvette with blood, which can react chemically with aluminium. Sheets of polycarbonate are used as windows. The cannulae that are used delivery tubes are held in place by delrine gaskets. Screwing the parts tightly together with the ten screws on the front seals the cuvette, see ***Figure 36***. All dimensions are given in mm.

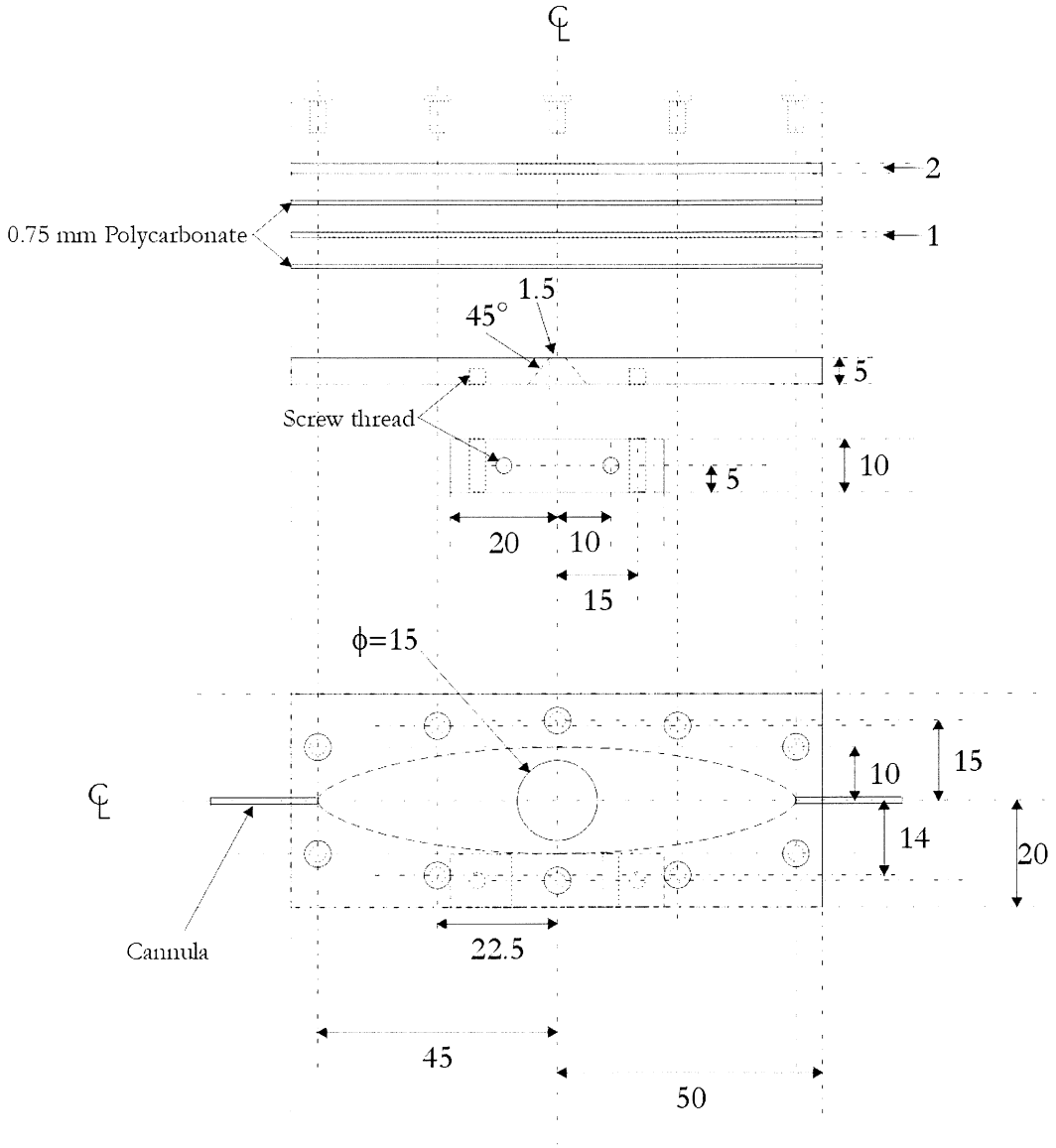

Figure 36: ***This drawing illustrates the design of the cuvette.***